Tidal triggering of low frequency earthquakes near Parkfield, California: Implications for fault mechanics within the brittle-ductile transition

A. M. Thomas,[1] R. Bürgmann,[1] D. R. Shelly,[2] N. M. Beeler,[2] and M. L. Rudolph[1]

[1] Studies of nonvolcanic tremor (NVT) have established the significant impact of small stress perturbations on NVT generation. Here we analyze the influence of the solid earth and ocean tides on a catalog of ∼550,000 low frequency earthquakes (LFEs) distributed along a 150 km section of the San Andreas Fault centered at Parkfield. LFE families are identified in the NVT data on the basis of waveform similarity and are thought to represent small, effectively co-located earthquakes occurring on brittle asperities on an otherwise aseismic fault at depths of 16 to 30 km. We calculate the sensitivity of each of these 88 LFE families to the tidally induced right-lateral shear stress (RLSS), fault-normal stress (FNS), and their time derivatives and use the hypocentral locations of each family to map the spatial variability of this sensitivity. LFE occurrence is most strongly modulated by fluctuations in shear stress, with the majority of families demonstrating a correlation with RLSS at the 99% confidence level or above. Producing the observed LFE rate modulation in response to shear stress perturbations requires low effective stress in the LFE source region. There are substantial lateral and vertical variations in tidal shear stress sensitivity, which we interpret to reflect spatial variation in source region properties, such as friction and pore fluid pressure. Additionally, we find that highly episodic, shallow LFE families are generally less correlated with tidal stresses than their deeper, continuously active counterparts. The majority of families have weaker or insignificant correlation with positive (tensile) FNS. Two groups of families demonstrate a stronger correlation with fault-normal tension to the north and with compression to the south of Parkfield. The families that correlate with fault-normal clamping coincide with a releasing right bend in the surface fault trace and the LFE locations, suggesting that the San Andreas remains localized and contiguous down to near the base of the crust. The deep families that have high sensitivity to both shear and tensile normal stress perturbations may be indicative of an increase in effective fault contact area with depth. Synthesizing our observations with those of other LFE-hosting localities will help to develop a comprehensive understanding of transient fault slip below the "seismogenic zone" by providing constraints on parameters in physical models of slow slip and LFEs.

1. Introduction

[2] Large slow-slip events in deep subduction zone environments are recorded geodetically, as periodic transient reversals of long term GPS velocities or tilt measurements, and seismically, as long duration, low frequency seismic signals, dubbed non-volcanic tremor (NVT) due to their similarity to volcanic tremor [*Obara*, 2002]. Though slow-slip and NVT occur simultaneously, inversions of GPS displacements during slip events in the Cascadia subduction zone result in strain release equivalent to M_w ∼6 events [*Schmidt and Gao*, 2010], while the total seismic moment of NVT are orders of magnitude smaller [*Kao et al.*, 2010]. Slip and tremor in subduction zone environments reflect slow-slip events (SSEs) that propagate along the subduction interface at velocities of ∼10 km/day and are largely confined to the region downdip of the locked subduction thrust [*Obara et al.*, 2004; *Dragert et al.*, 2004]. As these SSEs propagate, small

[1]Department of Earth and Planetary Science, University of California, Berkeley, California, USA.
[2]Earthquake Science Center, U.S. Geological Survey, Menlo Park, California, USA.

Corresponding Author: A. M. Thomas, Department of Earth and Planetary Science, University of California, 169 McCone Hall, Berkeley, CA 94720, USA. (amthomas@berkeley.edu)

on-fault asperities capable of generating seismic radiation fail in earthquake-like events or low-frequency earthquakes (LFEs). The collocated, coeval evolution of NVT, SSEs, and LFEs led *Shelly et al.* [2007a] to suggest that part if not all of the seismic signature of NVT could represent a superposition of multiple LFEs. Focal mechanism inversions of LFEs in Shikoku indicate that LFEs are a manifestation of shear slip located largely on the plate boundary [*Ide et al.*, 2007]; however other studies have reported intraplate NVT locations which may suggest they can take place on any localized slip surface if source region conditions are agreeable [*Kao et al.*, 2005]. Application of matched filter techniques to other subduction zones and tremor on the deep San Andreas fault (SAF) indicate that global observations of NVT can be explained as a superposition of many LFEs [*Shelly et al.*, 2007a; *Brown et al.*, 2009; *Shelly and Hardebeck*, 2010]. The similarities between LFEs in different tectonic settings suggests that the same slip phenomena that take place in subduction zone environments such as Cascadia and Shikoku may also occur on transform systems such as the SAF.

[3] In idealized models of deformation in fault zones, slip is accommodated in one of two ways: seismically, in earthquakes that occur in the shallow, brittle regions of the crust, or aseismically, in deep shear zones where pressure and temperature conditions are more amenable to ductile deformation. Shallow aseismic slip also occurs on some faults, however the mechanisms for this shallow creep may not be the same as those in deep faults [*Marone*, 1998]. The identification of highly episodic, non-volcanic tremor and slow slip below the seismogenic zone [*Hirose et al.*, 1999; *Dragert et al.*, 2001; *Obara*, 2002; *Miller et al.*, 2002] has modified our notion of seismic coupling and the relative partitioning between seismic and aseismic deformation. While aseismic slip is not explicitly hazardous there are implicit or indirect implications for hazard; deformation in deep fault zones transfers stress to shallow faults where large, devastating earthquakes can occur. Since shallow and deep slip are potentially related, developing a comprehensive understanding of fault zone anatomy, meaning where and how different slip mechanisms operate, the physics that governs deformation style, and stress transfer between the deep and shallow crust may mitigate seismic hazard.

[4] One characteristic common to global observations of NVT and LFEs is extreme sensitivity to small stress perturbations. Studies of static stress changes from regional earthquakes report both an aftershock-like response of deep NVT on the SAF to increases of 6 and 10 kPa in shear stress from the 2003 M_w 6.5 San Simeon and the 2004 M_w 6.0 Parkfield earthquakes respectively, and quiescent response to decreases in failure stress [*Nadeau and Guilhem*, 2009; *Shelly and Johnson*, 2011]. Several studies report triggering of NVT by teleseismic surface and body waves that imposed stress transients as small as a few kilopascals [*Gomberg et al.*, 2008; *Miyazawa and Brodsky*, 2008; *Peng et al.*, 2009; *Hill*, 2010; *Ghosh et al.*, 2009; *Shelly et al.*, 2011]. Additionally, studies of tidal stress perturbations conclude that NVT are sensitive to stress changes as small as fractions of a kilopascal [*Rubinstein et al.*, 2008; *Nakata et al.*, 2008; *Lambert et al.*, 2009; *Thomas et al.*, 2009; *Hawthorne and Rubin*, 2010]. While these stress changes are exceedingly small, a number of other geological phenomena including

volcanoes, landslides, and glaciers are influenced by kPa-level stress changes caused by the tides [*McNutt and Beavan*, 1984; *Schulz et al.*, 2009; *de Juan et al.*, 2010].

[5] Early investigations of tidal triggering of earthquakes find no relationship between earthquakes and tidal forcing [*Heaton*, 1982; *Vidale et al.*, 1998]. *Lockner and Beeler* [1999] and *Beeler and Lockner* [2003] used laboratory friction experiments and rate and state dependent friction theory to argue tides and earthquakes are correlated but catalogs with large event numbers are required to detect a very modest correlation and the degree of correlation increases as the ratio of the amplitude of the tidal shear stress to the effective confining stress increases. A number of later studies substantiate the latter point, most notably *Cochran et al.* [2004] find a robust correlation between tidal stress and earthquakes in shallow subduction environments (i.e. where the ocean tidal loads can be as large as 10 kPa and the confining stress is relatively low). High fluid pressures in both Nankai and Cascadia are inferred from the high V_p/V_s ratios in the NVT source region documented by *Shelly et al.* [2006] and *Audet et al.* [2009] which may explain the robust correlation of NVT to small stress perturbations. *Thomas et al.* [2009] show that NVT rates on the Parkfield section of the SAF vary substantially in response to small fault-parallel shear stresses induced by the solid earth tides and were only modestly influenced by the much larger fault-normal and confining stress cycles. *Thomas et al.* [2009] appeal to the presence of pressurized pore fluids in the NVT source region to explain their observations. They calculated effective normal stresses between 1 and 10 kPa suggesting that pore fluid pressures in the NVT source region are very near lithostatic.

[6] In this study we use the response of LFEs near Parkfield to tidally induced stress perturbations to infer mechanical properties of the LFE source region on the deep SAF. Previous studies of tidal modulation of NVT in Parkfield used start times and durations of NVT events in the catalog described by *Nadeau and Guilhem* [2009]. The present study utilizes the added spatial and temporal resolution gained in using matched filter and stacking techniques to identify and locate LFE families [*Shelly and Hardebeck*, 2010] to map the spatial variability of sensitivity to tidally induced stresses and effective stress. We present observations of the tidal influence on slip on the central SAF, inferences about properties of the LFE source region informed by those observations, and when possible, comparisons between our findings and relevant observations in other tectonic environments.

2. Data and Methods

2.1. Low Frequency Earthquake Catalog

[7] The 2001-January 2010 low-frequency earthquake catalog of *Shelly and Hardebeck* [2010] is composed of ~550,000 LFEs grouped into 88 different families based on waveform similarity. Locations of LFE families in Parkfield are tightly constrained by numerous P- and S-wave arrival times at densely distributed stations. The location procedure involves visually identifying individual LFE template event candidates and then cross-correlating and stacking those waveforms with continuous seismic data to detect other LFEs in the same family. The most similar events are stacked at all
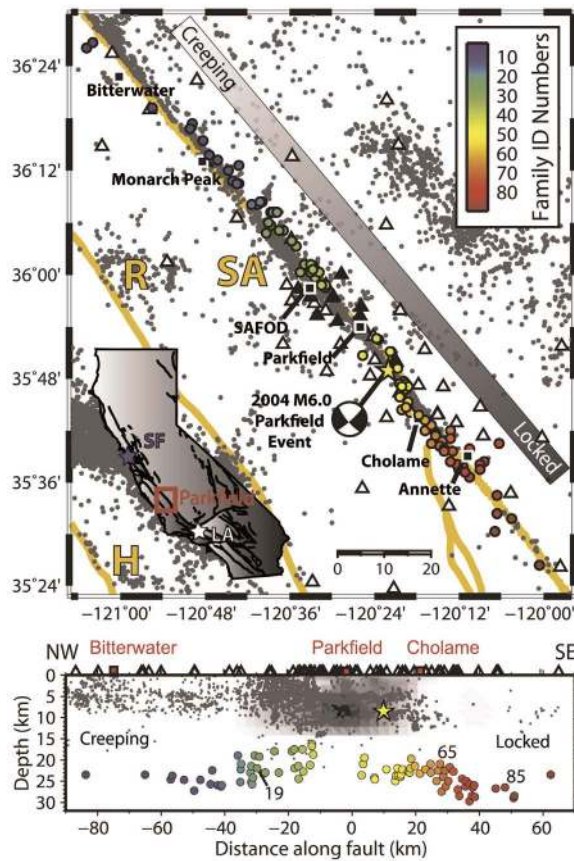
Figure 1. (top) Parkfield area location map with LFE locations are plotted as circles color-coded by family ID numbers organized from northwest to southeast along the fault. Relocated earthquakes (post 2001) from the catalog of *Waldhauser and Schaff* [2008] are shown as gray dots. The Hosgri (H), Rinconada (R), and San Andreas (SA) faults are shown in orange. Surface seismic stations used for detection and borehole stations used for location are shown by white and black triangles respectively. The September 28, 2004 M_w 6.0 Parkfield earthquake epicenter is indicated by the yellow star. Inset map shows area of map view marked in red and locations of San Francisco (SF) and Los Angeles (LA). (bottom) Along fault cross section of the San Andreas viewed from the southwest (vertical exaggeration is 4:3) showing locations of LFE families shown in top panel and color coded by their family ID number. Families that are highlighted in the text are labeled by their ID numbers. Relocated earthquakes shown in top panel within 10 km of the fault are plotted as gray dots. The slip distribution of the 2004 M6.0 Parkfield earthquake from *Murray and Langbein* [2006] is shown in shades of gray. Stations shown in top panel and relevant landmarks are indicated by triangles and red squares respectively.

regional stations, and P- and S-wave arrivals are identified on these stacked waveforms. LFEs are located by minimizing travel time residuals in the 3D velocity model of *Thurber et al.* [2006] with estimated location uncertainties of 1–2 km (for further details see *Shelly and Hardebeck* [2010]). Hypocenters of LFE families, shown in Figure 1, are distributed along

~150 km of the SAF from Bitterwater to south of Cholame. Estimated source depths extend from just below the base of the seismogenic zone to the Moho (16–30 km depth) on the deep extension of the SAF, a zone previously thought incapable of radiating seismic waves.

[8] Locations separate into two distinct groups: one to the northwest below the creeping section of the SAF, and one extending to the southeast from below the rupture area of the 2004 M_w 6.0 earthquake into the locked section of the fault that last ruptured in the 1857 Fort Tejon earthquake. These groups are separated by a 15 km gap beneath the town of Parkfield, where no tremor has yet been detected. The presence of a gap in the locations is not a product of station coverage or the location procedure. Very low tremor amplitudes on each side of this gap suggest that tremor amplitudes in this zone may simply fall below current detection thresholds [*Shelly and Hardebeck*, 2010].

[9] Tremor amplitudes (maximum recorded ground velocities) and recurrence patterns vary considerably, and semicoherently, along fault strike and with depth. The strongest tremor is consistently generated along a ~25 km section of the fault south of Parkfield, near Cholame [*Shelly and Hardebeck*, 2010]. Activity in some families is highly episodic, with episodes of very high activity concentrated within a few days, followed by 2–4 months of quiescence. An example of highly episodic behavior is shown in Figure 2, family 65, where individual slip events can host over 200 LFEs in a five day period. These punctuated episodes concentrate in several relatively shallow neighboring families whereas the deepest families (e.g. family 85 in Figure 2) recur frequently, with small episodes of activity as often as every 2 days with few intermittent periods of increased activity [*Shelly and Johnson*, 2011].

[10] Oftentimes adjacent or nearby LFE families have nearly identical event histories suggesting that they fail together and experience very similar stressing histories. Neighboring, highly-episodic families generally produce bursts of activity almost simultaneously [*Shelly et al.*, 2009]. In Parkfield, this observation is most robust in the shallowest families; however there is also evidence for interaction in deeper families that still occur episodically. If LFE recurrences track the rate of dominantly aseismic fault slip, then these episodes likely represent propagating slip fronts, analogous to slow slip events in subduction zone settings. No geodetic manifestation of deep slow slip episodes has yet been observed in Parkfield, and slow slip events on the deep San Andreas probably produce surface deformation that falls below the detection threshold for borehole strain, GPS or laser strainmeter instrumentation [*Smith and Gomberg*, 2009].

2.2. Tidal Model

[11] We compute tidally-induced strains at the centroid of the tremor source region (−120.525, 35.935, 25 km depth) using the tidal loading package Some Programs for Ocean Tide Loading, which considers both solid earth and ocean load tides [*Agnew*, 1997]. For the solid earth contribution, displacements are very long wavelength compared to the source region depth, thus we assume that the strains modeled at the surface are not significantly different from those at 25 km depth. Unlike the body tides, the strain field computed
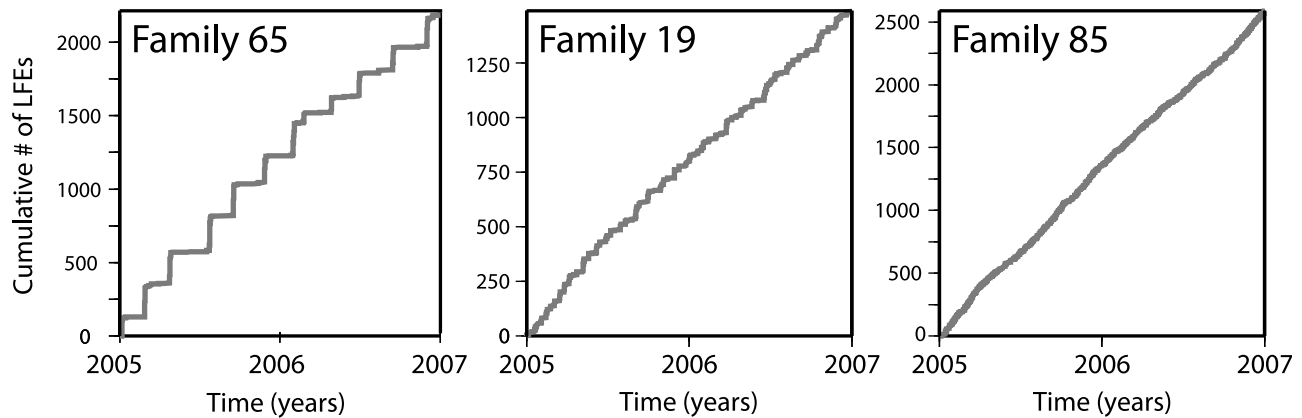
Figure 2. Example time series of cumulative number of LFEs over a two year time period for three LFE families (65, 19, and 85, see Figure 1 for locations in cross section). Family 65 is highly episodic with 2–4 month quiescent periods punctuated by few-day periods with extremely high LFE rates. In contrast, family 85 recurs frequently, with a general absence of quiescence and a few intermittent episodes of much smaller magnitude than family 65. Family 19 is an example of transitional behavior between the two end-member cases.

at the surface cannot be applied at depth, as the magnitude of the ocean loading component may change significantly between the surface and 25 km. To resolve this potential issue, we calculate depth dependent, spherical Green's functions using a finite element model of the layered earth model of *Harkrider* [1970] which we then use to compute the strains from only the ocean loading component at depth. A comparison of the load tides reveals that there are small amplitude and phase shifts between the load tides at zero and 25 km depth. However, once the load tides are superimposed on the solid earth tides, which are roughly an order of magnitude larger, the differences between the two become negligibly different.

[12] Given the degree two pattern of the tides, we assume that tidal stress changes are small over the ∼140 km section of the SAF under consideration and that a single tidal time series computed at the centroid of the LFE source region can be applied to all 88 hypocentral locations. To validate this assumption, we computed and compared volumetric strain time series at the center and ends of the LFE source region and found that the difference between the two time series has average and maximum values of 1% and 5% respectively.

[13] We compute the shear and normal stresses on the SAF by converting strain to stress using a linear elastic constitutive equation and resolving those stresses onto a vertical plane striking N42°W. The relevant elastic parameters were chosen to be equivalent to those in the top layer of the continental shield model of *Harkrider* [1970]. A representative 14-day time series of the fault-normal and right-lateral shear stresses, FNS and RLSS respectively, are shown in Figure 3. The vast majority of the stress amplitudes are due to only the body tides, as the ocean loading contribution diminishes with distance inland. The solid earth tides induce largely volumetric stresses thus the resulting shear stress on the SAF is approximately an order of magnitude smaller than the normal stress. We also note that while the shear and normal stress components are due to a common forcing function, they are not directly correlated (see section 2.4).

2.3. LFE Correlation With Tidal Stress

[14] For each LFE we can compute the tidally induced stresses at the time of the event, as event durations of ∼10 s are short relative to tidal periods [*Shelly and Hardebeck*, 2010]. To quantify the overall correlation with tidal loading, we first define the "expected number of events", or the number of events that occur under a particular loading condition assuming that LFEs occurrence times are randomly distributed with respect to the time. The degree of correlation is defined by the percent excess value (N_{ex}) defined as the difference between the actual and expected number of events divided by the expected number of events [*Cochran et al.*, 2004; *Thomas et al.*, 2009]. Positive N_{ex} values indicate a surplus of events and negative values, a deficit. Loading condition can refer to the sign of a given stress component or to a particular stress-magnitude range. The load components we consider for the remainder of this manuscript are the
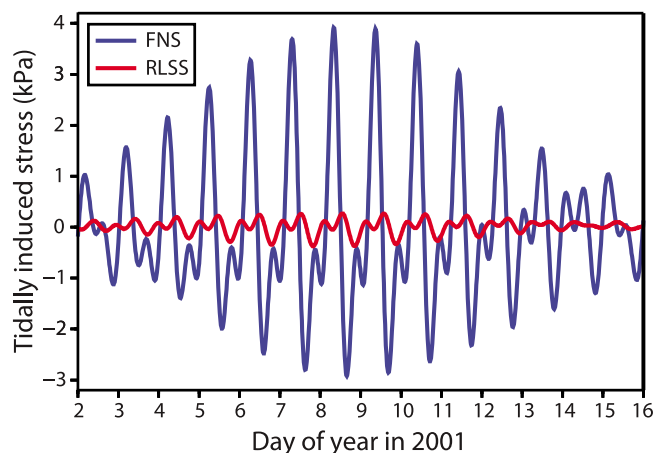

Figure 3. A representative 14 day time series of tidally induced shear (red) and normal (blue) stresses resolved onto the SAF striking N42°W.
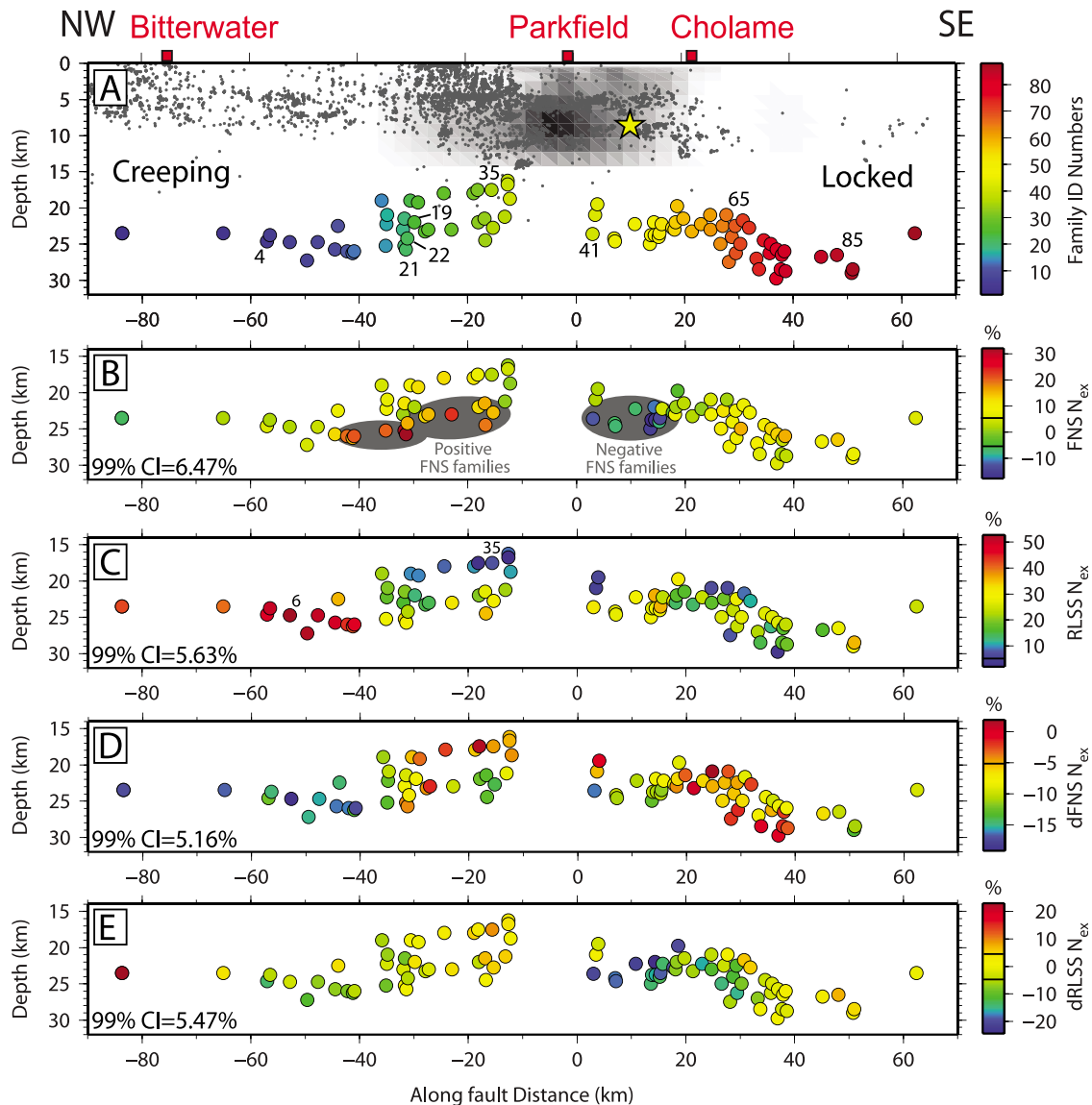
Figure 4. (a) NW-SE cross-section of LFE locations together with shallow microseismicity and slip distribution of the 2004 Parkfield earthquake from *Murray and Langbein* [2006]. (b–e) The locations of LFEs color-coded by the N_{ex} values corresponding to the tidal FNS, RLSS, dFNS, and dRLSS components calculated for the average fault strike of N42°W. 99% confidence intervals calculated for the family with the fewest events (largest uncertainty) are reported in the bottom left of each panel.

tidally induced fault normal stress (FNS), fault normal stress rate (dFNS), right-lateral shear stress (RLSS), and right-lateral shear stress rate (dRLSS). We compute N_{ex} values for all families relative to the sign of FNS, RLSS, dFNS, and dRLSS (shown in Figure 4). N_{ex} values corresponding to 99% confidence intervals are indicated in the lower left of each panel in Figure 4. Confidence intervals are computed by randomly selecting N times (where N corresponds to the number of LFEs in an LFE family) from the tidal time series to represent times of LFEs making up a synthetic catalog. FNS, RLSS, dFNS, and dRLSS N_{ex} values are then computed from the synthetically generated catalog. This process is repeated 25,000 times to construct N_{ex} distributions for each of the four stress components, which are then used to construct the two-sided 95% and 99% confidence intervals.

Confidence intervals as a function of N are shown in the auxiliary material (Figure S5).[1] The values reported at the 99% confidence intervals in Figure 4 correspond to the LFE family with the fewest number of LFEs. N_{ex} values different from zero by more than the 99% confidence level are less than 1% likely to occur by random chance assuming that tides and LFEs are not correlated.

2.4. Hypothesis Testing for Spurious Correlations

[15] One caveat of the aforementioned analysis is that each of the tidally induced stresses and stressing rates observed

---

[1]Auxiliary materials are available in the HTML. doi:10.1029/2011JB009036.

arises from a common forcing and thus they are inevitably related to one another (non-zero mutual information). However, the relationship between components cannot be characterized as a simple phase shift or amplitude scaling (Figure 3). Before interpreting the observed LFE sensitivities to tidal stress components we first address the potential for spurious correlations that have no physical meaning to arise due to the inherent correlation of the stressing functions. Artifacts can arise when one tidal component induces LFE occurrence due to some physical process and a second tidal component, which has no effect on LFE occurrence, is correlated with the first. In our interpretation of correlations of LFE timing to tidal stresses, we want to avoid interpreting spurious correlations in light of physical processes, which requires determining the sensitivity of tidal stressing components to one another.

[16] To test for spurious correlations, we use a bootstrap methodology to generate a large number of synthetic LFE catalogs based on the observed distribution of LFEs relative to a particular primary stressing function. These synthetic catalogs are then used to calculate confidence intervals for the expected N_{ex} values of the secondary stressing functions. To construct synthetic catalogs, we consider one stressing function (or null hypothesis) and one LFE family at a time. Instead of assuming LFEs are randomly distributed with respect to time as in the N_{ex} calculation, we assume (1) they are distributed in the way we observe for that particular component and (2) they are randomly distributed with respect to all other components. To construct the synthetic catalogs, we use the frequency distribution of LFEs relative to the primary stressing function, so each bin represents some range of stress and has a corresponding number of LFEs. For each bin, we randomly select an equal number of times out of the tidal time series that have stress values within the corresponding stress interval meant to represent times of LFEs in the synthetic catalog. We then compute the N_{ex} values for each of the secondary stressing functions based on this synthetic catalog of LFEs. We repeat this procedure 1000 times and use the resulting values to construct 95% and 99% confidence intervals. Finally, these confidence intervals are compared to the observed N_{ex} values for the secondary components.

[17] Models of frictional strength of faults depend on more than a single loading function, for example Coulomb failure strength is a function of both shear and normal stress. To test for this type of dependence, we also explore distributing synthetic catalog events randomly with respect to two different primary stressing components for a total of eleven different null hypotheses: one considering no correlation between LFEs and tides, four for each stressing component, and six for all possible combinations of two stressing components. The two component case is implemented with the same procedure as described above, except events are distributed relative to the joint frequency distributions of the two components. To quantify how well the null hypotheses characterize the remaining components, we define a misfit by determining the average number of standard deviations between the observed N_{ex} and 50th percentile of the synthetically derived N_{ex} values. For each family, the null

hypothesis that best characterizes the event times of that family is the one with the smallest misfit.

3. Results

3.1. Spatial Distribution of Sensitivity of LFEs to Tidal Stresses

[18] Since each family has more than 2,000 LFEs, we can calculate their sensitivity to tidal stresses at each location, which allows for a detailed view of the variability of tidal correlation with distance along the fault and depth. Figure 4 shows the along-fault cross sections of the locations of the 88 LFE families identified by *Shelly and Hardebeck* [2010] viewed from the southwest. Each family is color-coded by its sensitivity to the respective stressing condition (N_{ex} value). Sensitivities to all stressing components vary in a spatially coherent way, with nearby families often having similar triggering characteristics, along both strike and dip. To the northwest, within the creeping segment of the San Andreas, all but families 1 and 2 are either uncorrelated with the FNS or correlate with tensile FNS at a significance level of 99% or greater (panel B). The families with the highest FNS N_{ex} values are the deepest families that locate between −15 and −45 km along-fault distance from Parkfield (labeled Positive FNS families in Figure 4). The majority of families to the southeast of Parkfield are either not significantly correlated with the FNS or correlate in a less robust way than the highly correlated families within the creeping section (10% versus 30% N_{ex}). The notable exception to the overall correlation with tensile FNS is the localized group of families characterized by negative FNS N_{ex} values located along a 15 km-long stretch of fault beneath Parkfield. The results of the statistical analysis presented in section 3.2 indicate that the correlation with clamping is authentic as none of the null hypotheses are capable of explaining the observed deviation from zero as being due to inherent correlations with other stress components (see families 45–52 in Figure 5). These events are located along a releasing right bend of the SAF and variation in fault orientation provides a potential explanation for this correlation with clamping, which we discuss in section 4.6 [*Shelly and Hardebeck*, 2010].

[19] Correlation with positive, right-lateral shear stress (Figure 4c), is ubiquitous with all families correlating with shear stresses, which are an order of magnitude smaller than associated normal stresses, at a confidence level of 99% or greater. Again, triggering sensitivities vary in a systematic way, with the families that are most sensitive to shear stress fluctuations locating to the northwest below the creeping section. RLSS sensitivity in the families to the northwest of Parkfield appears to correlate with depth (Figure 4c). RLSS N_{ex} values transition smoothly from approximately 10% in the families between 16 and 20 km depth to values of 30% below, and reach nearly 50% in families further to the northwest at depths of up to ~28 km. The spatial pattern of RLSS N_{ex} values to the southeast of Parkfield appears to be more complex. The magnitudes of the dFNS sensitivity are about a factor of three smaller than the RLSS N_{ex} values. The spatial variation in dFNS mirrors that of the RLSS as families with significantly positive RLSS values also have significantly negative dFNS correlations (Figure 4d). The significance
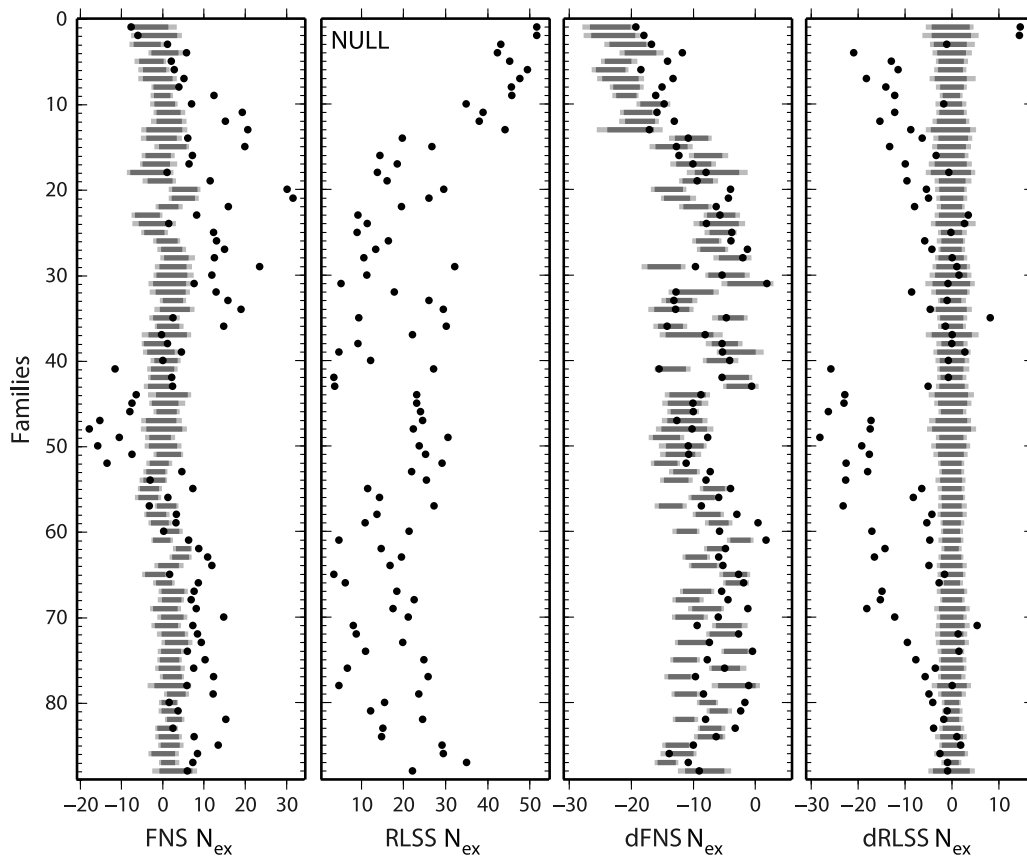
Figure 5. Results of bootstrap analysis with the null hypothesis that LFEs event times are influenced by the RLSS only. FNS, RLSS, dFNS, and dRLSS N_{ex} values for 88 LFE families are shown as black dots. Light and dark gray bars represent 95 and 99% confidence intervals derived from synthetic populations. The RLSS N_{ex} observations (marked NULL) have no confidence intervals because the synthetic catalogs are generated to match the RLSS N_{ex} values. Misfits are listed in Table S1 of the auxiliary material.

associated with the dFNS values is largely due to spurious correlation with RLSS as discussed in sections 3.2 and 4.5.

[20] Of the 88 LFE families, only five have statistically significant values of positive dRLSS at 99% confidence. Most dRLSS N_{ex} values are negative; that is, LFE are correlated with times of decreasing right-lateral stress. As shown in Figure 5, the correlation of LFEs with FNS may be partially responsible for the magnitude of the dRLSS N_{ex} values; however most of the correlation cannot be explained as a product of aliasing (see section 3.2 and Figure S1 of the auxiliary material). Within the creeping section of the fault, dRLSS values transition between statistically insignificant to around -10% N_{ex} values with depth/along strike from Parkfield to the northwest. Many of the most robustly correlated families are those within the fault-bend region to the southeast of Parkfield. However, several of the southeastern most families (along-fault distance of 20 km or greater) have significant negative values that are not associated with the bend.

3.2. Hypothesis Tests

[21] The hypothesis testing results for the one-component case of the RLSS are shown in Figure 5. Observed N_{ex} values for each of the four stressing components are indicated as black dots, while the 95% and 99% confidence intervals

derived by creating synthetic catalogs matching the RLSS distribution are shown in light and dark gray bars respectively. Figures 5 and S1 contain information about the relationship between the observed N_{ex} values and the tidal model, which can help to distinguish spurious and authentic correlations by minimizing the misfit between the observed N_{ex} values (black dots in Figure 5) and the 50th percentile of the confidence intervals generated from the synthetic populations for the eleven different null hypotheses. One principal result of the hypothesis testing procedure described above is that of the 88 LFE families, none is best described by the null hypothesis that LFEs are randomly distributed with respect to tides, meaning that at 99% confidence or greater one or more tidally induced stressing component is modulating LFE occurrence.

[22] A second important result is that LFE occurrence is most strongly associated with the RLSS. We come to this conclusion by considering that 73 of the 88 families are best characterized (lowest misfit) by the null hypotheses that either the LFE family members are preferentially triggered by the RLSS alone or that two components play a role in triggering, one of which is the RLSS. Of the 66 families that are best described by a two-component null hypothesis, 26 families are best described by the FNS-RLSS null hypothesis. These families preferentially trigger in response

to a tidal stressing function that incorporates some normal-stress dependence. The second and third most abundant groups of 17 and 15 families are best described by the RLSS-dFNS and the RLSS-dRLSS respectively. The dRLSS dependence of some families may be related to factors we will discuss in sections 3.6 and 4.6.

[23] The correlation of 17 families with both RLSS and dFNS is likely a spurious correlation. In Figures 5 and S1, the deviation of the computed confidence intervals from zero is a measure of how sensitive each component is to the null hypothesis in the tidal model, independent of the observations and the sign of the deviation relative to the value of the primary component from which the distributions were generated. If the observed N_{ex} values fall within the bounds of the computed confidence intervals then the correlation between the LFEs and the secondary stressing functions may be an artifact. If, on the other hand, the observed N_{ex} values fall outside the computed confidence interval, then they cannot be explained as a spurious correlation, or aliasing resulting from the component or components used as the null hypothesis. In Figure 5, confidence intervals for the FNS and dRLSS are mostly centered on zero suggesting little to no correlation with the RLSS. This is to be expected for the dRLSS, as when the RLSS is positive, half the time the dRLSS is also positive and half the time it's negative which should result in a distribution centered on zero. However, this is not the case for the dFNS, as almost none of the confidence intervals are centered on zero, indicating that the value of the dFNS is quite sensitive to the RLSS value. The extreme sensitivity of the dFNS values to the RLSS null hypothesis suggests that while the dFNS N_{ex} values for many LFE families are statistically significant relevant to the null hypothesis that there is no correlation between LFEs and tides, this significance is likely a spurious correlation caused by the robust correlation of those families with the RLSS. Hence, many of the observed dFNS N_{ex} values can be explained by accounting for this sensitivity (in Figure 5, observed dFNS N_{ex} falls within the 99% confidence range). The correlation between the RLSS and the dFNS is also evident in the observed N_{ex} values (Figure 6). The coefficient of determination, R^2, resulting from a linear regression of the RLSS and dFNS N_{ex} values is 0.66 indicating a robust correlation between the two (see Table S2 in the auxiliary material for associated significance values).

[24] While Figures 5 and 6 clearly demonstrate the sensitivity of dFNS to RLSS in the tidal model, there are significant correlations of some LFE families that cannot be explained by matching only the RLSS. Even the best fitting one or two-component hypotheses may have observations that lie outside of the generated confidence intervals. This discrepancy could be due a number of factors including unmodeled stress influences and assumptions such as fault orientation that go into our model of tidal stresses on the SAF. For these reasons, we do not require that the observed N_{ex} values for all families fall within the generated confidence intervals from a given hypothesis, but we simply consider the best-fitting hypothesis the one that minimizes the misfit between the data and the models (or hypotheses). For the remainder of this analysis, N_{ex} values are reported with respect to the null hypothesis that LFEs have no correlation with tidally induced stress, as they are a good metric for reporting the sensitivity of LFEs to tidally induced stresses and can be compared between components.

3.3. Tidal Sensitivity as a Function of Recurrence Interval

[25] *Hawthorne and Rubin* [2010] document the contemporaneous increase of tidal stresses on the plate interface and measured surface strain rates due to accelerated slip in the Cascadia subduction zone. Using this result, they inferred that tides are capable of modulating the slip rate of SSEs [*Hawthorne and Rubin*, 2010]. More recent studies of spatiotemporal characteristics of slow-slip fronts find that in addition to quasi-continual slip front advance, rapid back-propagating slip pulses, called rapid tremor reversals, are also apparent [*Houston et al.*, 2011]. Rapid tremor reversals may also be tidally correlated [*Houston et al.*, 2011], which suggests that tidally correlated strain rates could be caused by tidal influence on the slip velocity, slip front advance, or both. Recent studies of slip in Cascadia argue that slip and tremor are spatially and temporally coincident; hence NVT can be considered a proxy for the location of deep fault slip [*Bartlow et al.*, 2011]. If we extend this result to Parkfield, we may be able to gain additional insight into the mechanics of slow-slip fronts by using the recurrence times within respective families to separate the catalog into two end-member groups: LFEs that represent the initiation of slip on a particular asperity following a slip hiatus, and those that occur either as part of an ongoing episode (intra-event LFEs) or between episodes. We then examine the tidal correlation of these different populations which allows us to assess whether tides modulate the slip rate and/or the slip front velocity.

[26] The majority of LFE families have average recurrence intervals less than three days, including both the deep, constant rate families with repeat times averaging two to three days and intra-event LFEs that occur in the shallow episodic families with repeat times of much less than one day. We can distinguish initiating LFEs, or those that signal when a creep pulse arrives at an LFE hypocenter, from those that take place either as part of a creep event or those that occur in more continuous families (e.g. family 85 in Figure 2) by filtering LFEs as a function of the duration of the preceding recurrence interval, t_r. The population of LFEs with large values of t_r, should largely consist of initiating LFEs. A small fraction of events within the most episodic families do occur between large creep events so to further distinguish initiating events, we also require that the time between a particular LFE and the subsequent LFE be less than one day to exclude such events.

[27] The results of this analysis are shown in Figure 7, which plots the FNS and RLSS N_{ex} values for each population of events with recurrence intervals greater than t_r. For small values of t_r (minute timescales) nearly all events in the catalog are included, as indicated by the y-axis in Figure 7. As t_r increases, first the events with very short recurrence intervals, such as those that within the slip episodes experienced by families 19 and 65 (Figure 2) are filtered followed by events that take place as part of the deep, continuous families such as family 85 (Figure 2) which correspond to multiday t_r values. Finally, at many day timescales, initiating LFEs in families of intermediate episodicity are also filtered out leaving only the initiating LFEs in the highly episodic
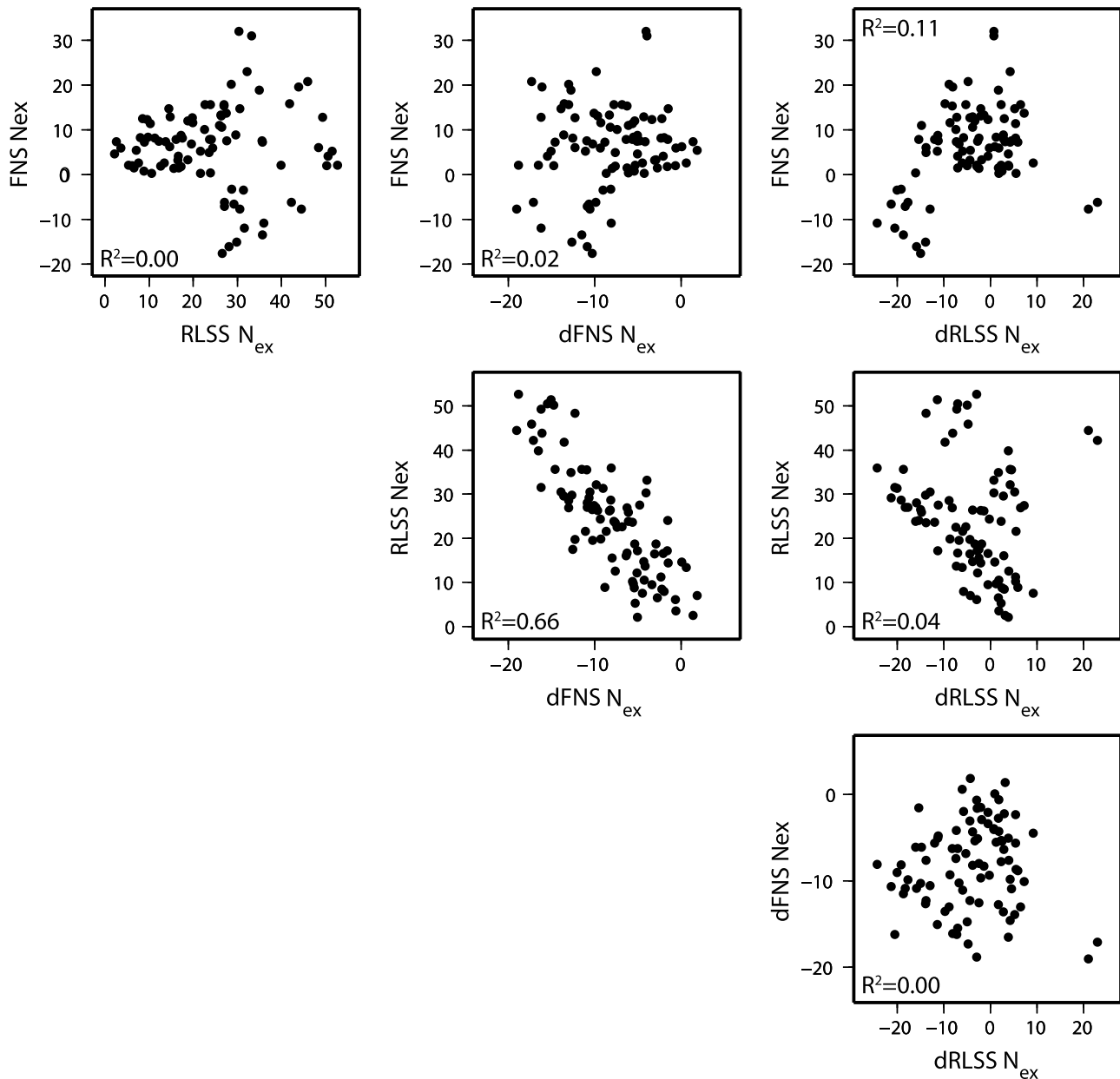
Figure 6. All possible combinations of N_{ex} values plotted against one another. Associated R^2 values are shown on each plot. The highest R^2 value, 0.66, suggests a spurious correlation may exist between the RLSS and dFNS components.

families. The corresponding RLSS N_{ex} values appear to decrease systematically with increasing t_r but remain significant over a wide range of interval durations. As the size of each population of events decreases with increasing t_r, the N_{ex} confidence intervals associated with each population shown in panels A and B grow wider. The FNS and RLSS N_{ex} values fall above the 99% confidence intervals for correlation until 43 and 25 days respectively. Slip events in Parkfield appear to vary in size, pattern, and duration, so it is difficult to place a definitive t_r cutoff to differentiate initiating events from all others. The most episodic families have average inter-episode periods of ∼60 days and episodes at a given family typically last ∼5 days. While the 43 and 25 day values are less than the average inter-episode period, they are

much greater than the average duration of a creep event in a highly episodic family. This result indicates that the population of LFEs that occur when a creep event arrives at an LFE hypocenter is correlated with both positive RLSS and tensile FNS. We discuss the implications of this finding in section 4.2.

3.4. LFE Rate Variation as a Function of Tidal Stress Magnitude

[28] In addition to quantifying the influence of tidal stresses on LFEs in the binary sense (Figure 4), we further explore how specific stress levels influence LFE production by computing LFE rates as a function of the magnitude of the applied stress. Figure 8 is constructed by dividing the
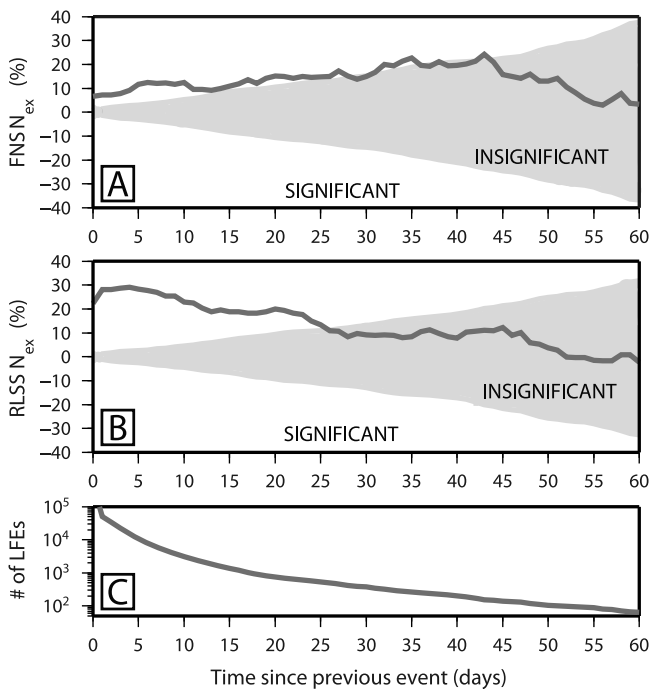
Figure 7. (a and b) The FNS and RLSS N_{ex} values (dark gray lines) calculated for all LFE events whose preceding recurrence interval is longer than the respective x-axis value (t_r). White background color represents N_{ex} values that are statistically significant at the 99% confidence level while values in the gray region are statistically insignificant. (c) The number of events in each population; since population size rapidly decreases with t_r, 99% confidence regions in Figures 7a and 7b grow larger. Note that the ~450,000 LFEs corresponding to the shortest time intervals are not shown.

observed number of LFEs for a particular family that fall within a given stress range for the stress component under consideration by the expected value based on the null hypothesis that LFEs and tides are randomly correlated. The resulting quantity is equivalent to $1 + N_{ex}$ for each stress bin. This process is repeated for each stress range of a given stress component and for all families. In Figure 8, the ratios of actual to expected number of LFEs are color-coded so values above one (warm colors), indicate a surplus of LFEs in that particular stress range and ratios below one (cool colors) indicate a deficit relative to the expected value. The abundance of values near one for the FNS plots confirms most families are generally not strongly influenced by the fault normal stress (or at least not to the degree of the RLSS). A few notable exceptions include families 19–22 and 26–29 which have LFE surpluses that correlate with peak tensile FNS. In addition, families 41, 44, 45, and 49–57 correlate with fault-normal clamping. In contrast to the FNS, substantial modulation of LFEs by the RLSS is almost ubiquitous for all 88 LFE families and well correlated with the stress magnitudes. Correlation between the stress amplitude and LFE rates is strongest in families 1–13, with a smooth rise of LFE rates with increasing RLSS. For families with strong RLSS correlation, LFE families are nearly quiescent when tidal stress is negative, with ratios near zero for RLSS less than −100 Pa.

[29] The results of the hypothesis testing analysis reported in section 3.2 indicate that the majority of the deviation of the dFNS N_{ex} values from zero is a spurious product of the robust correlation with RLSS. The correlation between triggering patterns of RLSS and dFNS are fairly evident in the 2nd and 3rd panels of Figure 8 with families with rate ratios that systematically increase as a function of the RLSS (gradual transition from blue to red) having a large excess number of events at negative values of dFNS (transition from tension to clamping). This is most evident in families 1–13, 32–36, and 47–54 however there are counterexamples, such as 69–74, that have LFE deficits at low dFNS values, despite robust correlation with RLSS.

[30] We reserve the detailed analysis of the dRLSS dependence for section 3.6, however, to first order an excess number of LFEs occur when dRLSS values are negative (i.e. with decreasing stress magnitude). For most families with significant dRLSS dependence, the highest ratios of actual to expected number of LFEs occur at negative but not extreme rate values.

3.5. Optimal Fault Azimuth for Tidal Correlation and the Role of Friction

[31] Tidal stresses are largely volumetric with a very small deviatoric contribution. For this reason, the FNS and dFNS N_{ex} values are relatively insensitive to the choice of fault azimuth, while the RLSS and dRLSS substantially change as a function of the assumed strike of the fault. *Thomas et al.* [2009] found that when the azimuth of the plane onto which the tidal stresses were resolved was allowed to vary, the orientation that maximized the excess percentage of NVT relative to the expected number of events was W44°N, parallel to the SAF strike. To further explore azimuthal dependence, we determine the optimal azimuth for each LFE family by finding the fault orientation that maximizes the number of LFEs that occur when tidally induced stresses promote slip in a right-lateral sense. To characterize the stressing function we consider two different friction coefficients: $\mu = 0.1$ and $\mu = 0$ or purely right-lateral shear stress dependence. Low friction values are suggested by the strong dependence on RLSS and optimal correlation of tidal stress and tremor at $\mu = 0.02$ found by *Thomas et al.* [2009]. If we consider μ values greater than 0.1, the order-of-magnitude higher FNS stresses dominate the change in Coulomb failure stress, resulting in substantially reduced N_{ex} values and sometimes spurious orientations of peak correlation azimuths. Figure 9 illustrates the dependence of N_{ex} on fault azimuth and μ for four example families. Family 4 located along the creeping SAF shows maximum correlation ($N_{ex} = 48\%$) at $\mu = 0$ and azimuth of N40°W. As the assumed friction value increases above 0.2 N_{ex} values drop to less than 20% with the optimal azimuth remaining roughly aligned with the SAF. Family 21 is part of a deep-seated group of sequences with significant correlation with RLSS and with tensile FNS. Peak correlation occurs at low friction values but N_{ex} values remain significant at greater values of μ for all orientations due to the small variation of FNS with azimuth. The shallow family 65 shows peak correlation ($N_{ex} = 10\%$) for fault azimuths of N30-40°W and $\mu = 0$. However, when higher contributions of FNS are considered, the orientation of peak correlation becomes highly variable and N_{ex} values fall to below 5% and are not statistically significant. Family 41 is
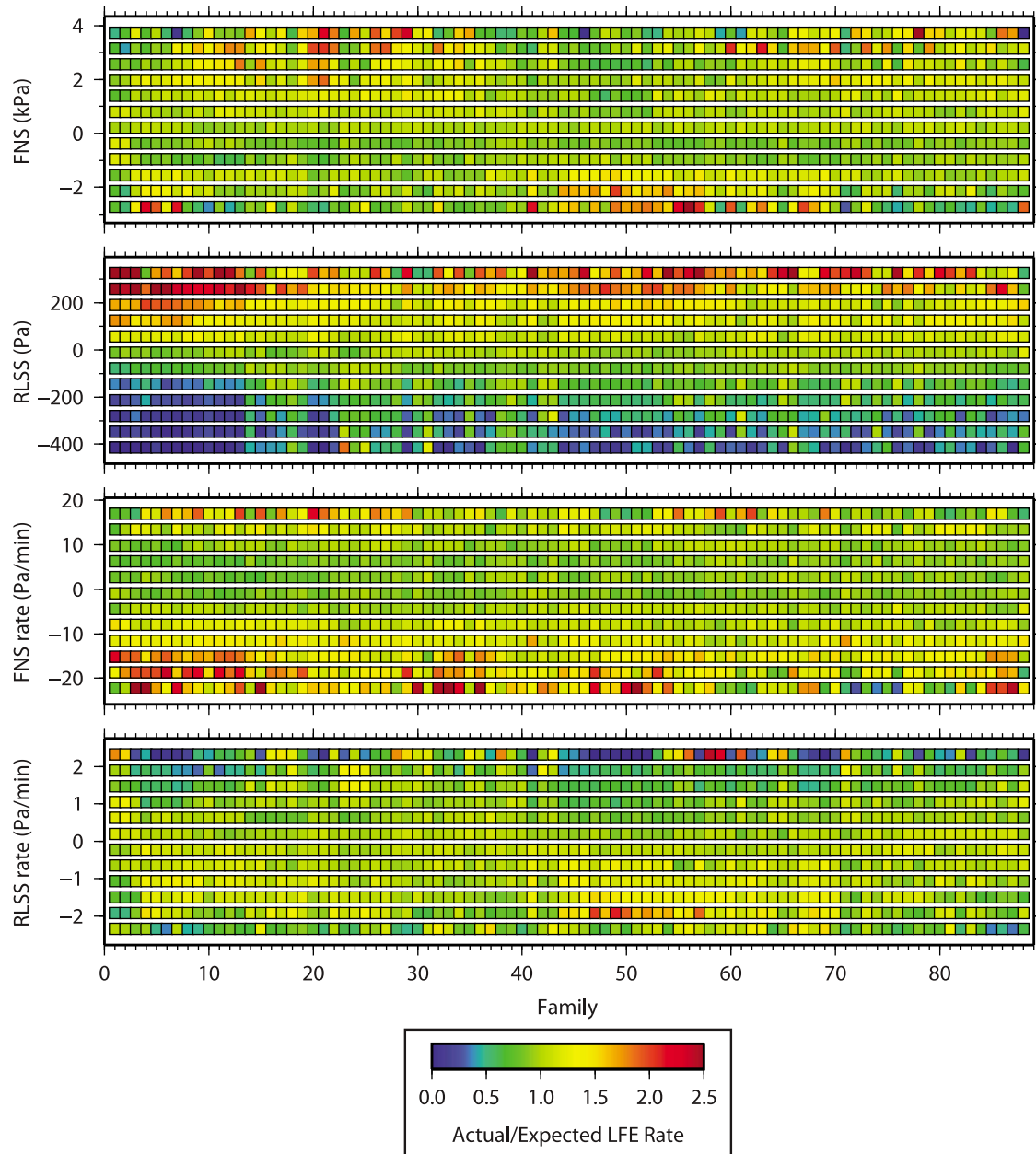
Figure 8. LFE rate plots for each tidally induced stressing component. Panels correspond to fault-normal stress, right-lateral shear stress, and their respective rates. Each column corresponds to an individual LFE family and each row, a stress interval. Each square is color-coded by the ratio of the actual number of LFEs within a given stress range over the expected number of LFEs that should occur within that range if tides and LFEs are uncorrelated (this reflects the amount of time the tides spend in the given range assuming a constant rate of LFE production). Cool colors represent a deficit of LFEs in the respective bin while warm colors indicate a surplus.

located along a right bend in the SAF and belongs to a group that exhibits pronounced correlation with compressional FNS. We again find peak correlation at zero friction along N40°W. As the contribution of FNS to the failure function is increased, N_{ex} values decrease but do not show a strong change in their spatial distribution. Peak N_{ex} values are generally found at very low or zero μ values. As tidal FNS is about an order of magnitude greater than RLSS, the correlation rapidly decreases with increasing μ. Corresponding plots

for all 88 families are shown in Figure S2 of the auxiliary material.

[32] Figure 10 shows the optimal orientation and corresponding Coulomb stress N_{ex} values for $\mu = 0$ and $\mu = 0.1$ showing lines aligned with the optimal orientation centered on the respective LFE hypocenter and circle colors indicating the corresponding N_{ex} values. The mean and standard deviations for both populations are reported in the bottom left of Figures 10a and 10b. One immediately obvious feature for both friction coefficients is the tight clustering of the axes
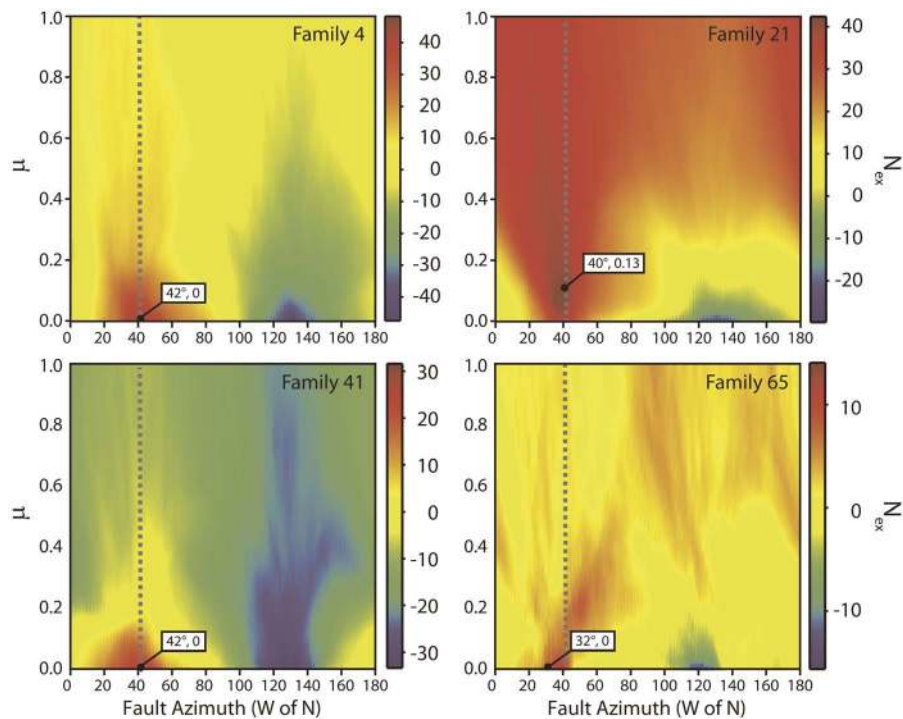
Figure 9. N_{ex} values as a function of azimuth and friction coefficient, μ, used to calculate tidal Coulomb stress (CFF = RLSS + μFNS) for four families (4, 21, 65 and 41 see Figure 4a for locations). Vertical line indicates the average local strike of the SAF (N42°W) and a black dot indicates peak N_{ex} for Coulomb stressing.

around the average orientation of the San Andreas (N42°W). A few families' peak-correlation orientation diverges from the fault strike by as much as 30° counterclockwise. The optimal orientation for these families more closely aligns with the San Andreas when we consider the modestly raised friction coefficient.

3.6. Phase of LFE Failure Times Relative to Tidal Load

[33] An effective tidal phase is assigned to each LFE by normalizing the magnitude and rate of the FNS and the RLSS at the time of the event by the absolute value of the most positive (or negative depending on the sign) value the stress
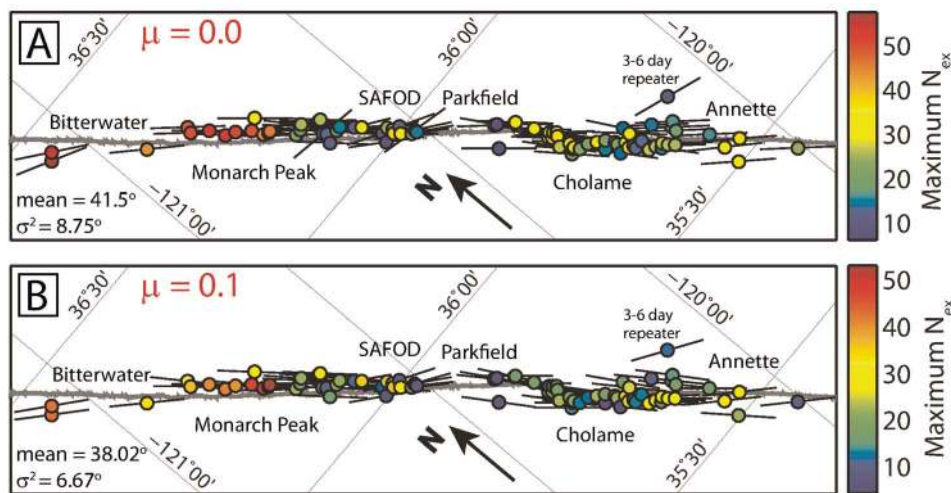

Figure 10. Rotated map view of SAF with LFE hypocenters color-coded with respect to N_{ex} value corresponding to the optimal orientation. Optimal orientations, defined as the orientation that maximizes the N_{ex} value, for each family are shown as black lines centered on the respective LFE hypocenter. Friction coefficients of (a) 0 and (b) 0.1 demonstrate the sensitivity of the optimal orientation to choice of friction coefficient. Mean orientations in degrees west of north and standard deviations for all families are shown in bottom left corner.
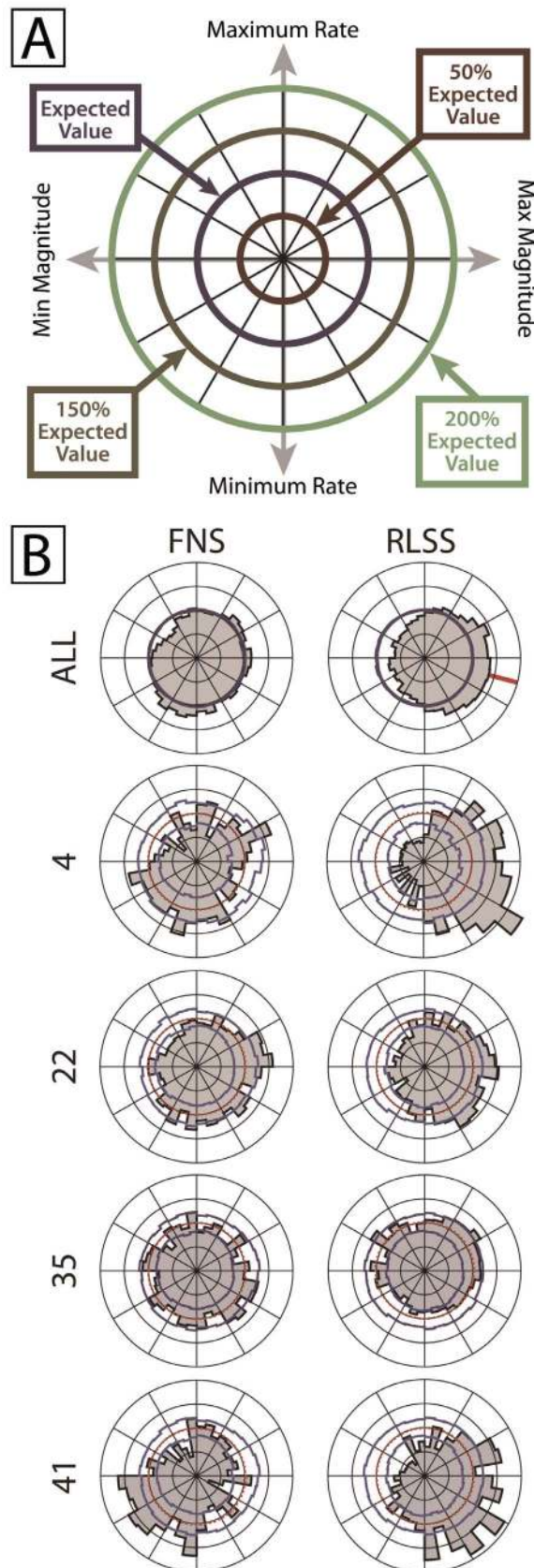
or stressing rate can attain. In this way, x- (magnitude) and y-values (rate) range between −1 and 1 and a phase value can be obtained for each event. A phase of zero (up) corresponds to the maximum rate and zero magnitude, a phase of 90 corresponds to maximum magnitude and zero rate, etc. Polar histograms are constructed by grouping the phases of all LFEs within a particular family in 10 degree bins and then normalizing each bin by the number of events expected to occur in that range based on the tidal stress distribution. Thus, the radial dimension of the histogram is the actual over the expected number (N_{ex} + 1) of events for that particular range of phases (expressed as a percentage in Figure 11a). A bin that contains the number of LFEs expected based on the tidal distribution has a radius of one (i.e. the expected 100% value assuming no tidal triggering). The full radial dimension of the phase plots corresponds to double the expected number of events.

[34] Results for example families 4, 22, 35, 41 (locations labeled in Figure 4a), and the complete catalog are shown in Figure 11 (see Figure S3 of the auxiliary material). Family 4 generally shows very weak FNS dependence and extreme sensitivity to tidally induced RLSS (RLSS N_{ex} value of 48%), which is evident from the phase plots in Figure 11b. Radial values on the right half of the diagram corresponding to positive magnitude are almost entirely above the expected value, with a corresponding depletion of LFEs during negative magnitude RLSS on the left half of the plot. The event excess also seems to be rate dependent as evidenced by the post-maximum magnitude RLSS peak which indicates preferential failure during times of moderate negative dRLSS.

[35] Family 22 is an example from the cluster of deeper families with moderate to strong RLSS correlation (23% RLSS N_{ex}) also characterized by preferential failure during times of extensional normal stress (16% FNS N_{ex}). The FNS phase plot for family 22 shows preferential failure during times of peak-positive FNS. Family 22 also has a substantial positive RLSS dependence which may explain why there are sometimes more events than expected during times of negative (compressive), decreasing FNS. The correlation with decreasing FNS is likely due to the aliasing effect between the RLSS and dFNS mentioned in section 3.2. Family 35 is shallow and less sensitive to tidally induced stresses as evidenced by the majority of bins within the phase plot falling near the expected value, within the 99% confidence bins. Family 41 (−12% FNS N_{ex}, 32% RLSS N_{ex}) is a member of the anomalous group of families that fail preferentially during times of negative FNS. The correlation with negative, decreasing FNS is apparent in the phase plot of family 41. In family 41 events cluster with broad peak in the positive,

Figure 11. (a) A schematic phase plot labeling the 50%, 100%, 150% and 200% expected value contours. (b) FNS (left) and RLSS (right) phase plots for a stack of all events in the catalog and four example families (4, 22, 35, and 41). Gray shaded areas indicate ratio of observed to expected number of events in each 10 degree phase bin. Thin dark blue lines are 99% confidence intervals for each population. Thin dashed red lines are 100% expected value contours. The solid red line in the RLSS phase plot for the bulk catalog marks the half hour phase shift discussed in the text.

decaying RLSS and strong FNS peak in the quadrant of increasing compression.

[36] Families 4 and 35 represent two end-member types of behavior; however, some families have patterns that are not as readily interpretable. The general correlation of all families within the catalog to RLSS is apparent in the stacked phase plot of all LFEs within the catalog. The large number of events ($N = 544,369$) reduces the confidence intervals to very near the expected value, hence any deviations from that value are highly significant. If LFEs correlated with only RLSS magnitude, then we would expect the region that exceeds the expected value to be symmetric about the magnitude axis. However, the phasing of failure times with respect to RLSS seem to be phase dependent, as the majority of LFEs fail during times of large, positive RLSS magnitude and small, negative dRLSS which produces an ∼30 minute phase shift in the time of the peak radial value with respect to the peak RLSS. This effect is also apparent in the dRLSS N_{ex} values reported above and shown in Figure 4e. Families that are highly sensitive to negative FNS are generally most robustly correlated with negative dRLSS. However, these families are not solely responsible for the apparent phase shift as the same dRLSS dependence is still present when we iterate the analysis while excluding families correlated with negative FNS. We discuss the possible causes of this apparent phase shift in the correlation with tidal RLSS in section 4.5.

4. Discussion

[37] As the most studied continental transform environment known to host tremor and transient fault slip, diagnostic observations of slow slip in Parkfield complement those in subduction zones providing additional information about the mechanics of slip in deep fault zones. Full azimuthal station coverage, a high-resolution seismic network, and detailed waveform analysis help us better constrain the location and timing of individual LFEs in Parkfield. If the same underlying physics for slow-slip generation applies to both subduction zone environments and continental settings, then the observations of LFEs in Parkfield may aid in developing generally applicable models of SSEs not limited to tectonic environment. In this section we discuss the implications of the results presented in section 3.

4.1. Spatial Distribution of Tidal Sensitivity and LFE Episodicity

[38] Our observations of tidal modulation of LFEs in Parkfield is generally consistent with previous studies that report statistically significant influence of the ocean and solid earth tides on slow slip and NVT in subduction zones [*Rubinstein et al.*, 2008; *Nakata et al.*, 2008; *Lambert et al.*, 2009; *Hawthorne and Rubin*, 2010; *Ide*, 2010]. The enhanced spatial and temporal resolution afforded by studying LFEs allows us to map the spatial variability of tidal influence and infer from those observations the spatial heterogeneity of fault mechanical properties. We are able to separate the contribution of shear and normal stress components and their rates to the triggering.

[39] The majority of LFE families are highly correlated with RLSS, however the spatial variability of tidal correlation below the creeping and locked sections of the SAF has different characteristics. Along the creeping section of the

SAF to the northwest of Parkfield, the correlation systematically increases from less than 10% N_{ex}, below the Parkfield earthquake at 16 km depth, to above 50% N_{ex} with both distance to the northwest and depth. To the southeast of Parkfield RLSS N_{ex} values continue to be high, but their spatial distribution is more complex with substantial along-fault changes and lack of a consistent change with depth (Figure 4c). A number of factors can influence the sensitivity of LFE sources to small stress perturbations, however, the magnitudes of the RLSS sensitivity in nearly all families require that elevated pore fluid pressures be present on the deep SAF (section 4.3). Most families are weakly correlated with positive FNS, however there are two groups of families that correlate with positive and negative FNS (labeled in Figure 4b). From the analysis presented in section 4.2, and due to the spatially localized nature of these groups, we believe these correlations are not artifacts. We discuss potential causes of the negative and positive FNS N_{ex} values in sections 4.6 and 4.7 respectively.

[40] Study of LFEs also allows for a more detailed assessment of the relationship between the distribution of LFEs in time (i.e. episodic versus continuous) and tidal influence. To quantify the episodicity of individual LFE families, *Shelly and Johnson* [2011] used the minimum fraction of days required to contain 75% of all events within a family (MFD75). Highly episodic families (e.g., 65 in Figure 2) are characterized by MFD75 values around zero while continuous families (e.g. family 85 in Figure 2) have values around 0.25. The relationship between episodicity, depth, and tidal modulation is shown in Figure 12. We find that highly episodic families with bursts of LFEs interspersed with episodes of quiescence are less tidally influenced than the deeper, continuously deforming families. Families with low MFD75 values tend to be shallower and have either insignificant or small N_{ex} values when compared with the rest of the catalog. If we consider the fault essentially locked during quiescent periods with the punctuated LFE bursts representing times when the fault is slipping at the particular hypocenter, then weaker tidal modulation may suggest the magnitude of tidal correlation decreases during strongly accelerated fault slip, as the stress applied to any asperity due to an accelerated background slip rate is likely much larger than the tidal stress contribution. More continuously active LFE families (high MFD75 values in Figure 12) show a wide range of N_{ex} values in both FNS and RLSS components that suggest that other factors can dominate the degree of tidal correlation.

[41] There are similarities and differences with the temporal and spatial patterns of tremor found in subduction zones. *Ide* [2010] explored the relationship between tremor and tidal sensitivity in Shikoku, and found a correlation between deformation style, depth, and tidal influence. At Shikoku, the longer-lasting tremor events occur at greater depths in small and frequent episodes while the duration of shallow NVT events are shorter and occur primarily during large and infrequent tremor episodes, two or three times per year [*Obara*, 2010; *Ide*, 2010]. However, to first order the sensitivity to tidal stress appears to be strongest in the shallow portions of the tremor region at Shikoku, in contrast to our results [*Ide*, 2010]. *Ide* [2010] did not explicitly model the distribution of tidal stresses in space and time so it is difficult to ascertain if the distribution in tidal sensitivity
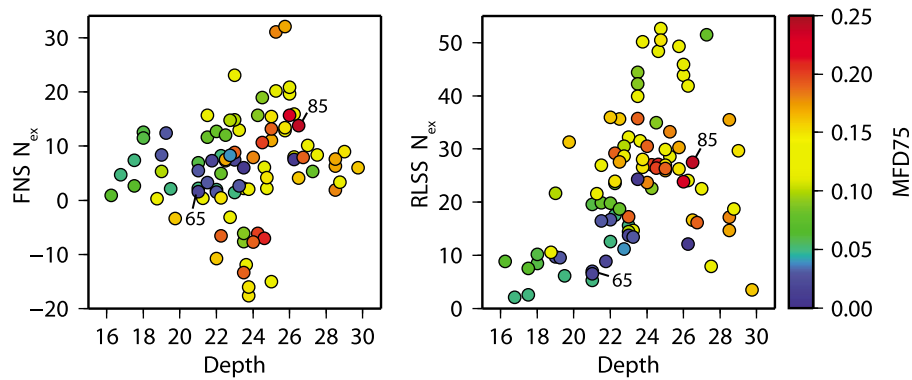
Figure 12. Variation in FNS and RLSS N_{ex} values for all LFE families plotted as a function of depth. Families are color-coded by their MFD75 value from *Shelly and Johnson* [2011]. Lower MFD75 values correspond to highly episodic families while higher values correspond to more continuous families. The shallow and episodic family 65 and deep and continuous family 85 shown in Figure 2 are labeled.

reflects differences in tidal stress or source region behavior. Further comparisons are difficult to make due to the application of different detection and location methodologies. Smaller tremor episodes without geodetically detectable slow slip identified in Cascadia [*Wech et al.*, 2009; *Wech and Creager*, 2011], Mexico [*Brudzinski et al.*, 2010], and Oregon [*Boyarko and Brudzinski*, 2010] also occur downdip of the section of the megathrust that hosts larger SSEs. This suggests a transition from highly episodic to continuous deformation with depth in those locations, which is qualitatively consistent with Parkfield. Correlation with tidal stress has so far only been documented during large and shallow SSEs in Cascadia [*Rubinstein et al.*, 2008; *Lambert et al.*, 2009; *Hawthorne and Rubin*, 2010]. Future work should evaluate to what degree tidal sensitivity of tremor changes with depth and/or size and recurrence interval of NVT episodes in these areas.

4.2. Slip Front Propagation and Slip Velocity

[42] We motivated section 3.3 by asking if increased strain rates during periods when tides are encouraging slip were due to tidal modulation of slip velocity or tidal influence on slip front velocity [*Hawthorne and Rubin*, 2010]. Since most of the very episodic LFE families have statistically significant RLSS N_{ex} values, and the vast majority of LFEs within these families occur during slip events, we can confirm that slip rates are tidally modulated during an ongoing slip episode. The modulation of LFE rates in the presence of an ongoing slip episode suggests that the slip velocity is tidally modulated, consistent with the findings of *Hawthorne and Rubin* [2010] for the Cascadia SSEs.

[43] To address whether tides also control slip front or propagation velocity we analyzed the tidal correlation of LFE populations filtered by the duration of the preceding recurrence interval t_r (Figure 7). The majority of LFEs with large prior recurrence intervals represent the first event in an episode at a family location, and thus may indicate when a creep front arrives at the location of a particular LFE hypocenter. From our analysis in section 3.3, we find that the population of LFEs following a quiescence of several days are still strongly tidally correlated. So why should the first seismic signature of a slip pulse at an LFE family hypocenter correlate with the tides? One possibility is that creep front propagation is tidally controlled; meaning the shear and normal stress perturbations are of sufficient magnitude to accelerate or decelerate the advance of the slipping region of a fault. If is were true, slip fronts may advance faster during times when tides are inducing stresses favoring slip front propagation. At present, geodetic studies of the spatiotemporal progression of slip in Cascadia are not of sufficient precision to resolve if slip front propagation speeds are tidally controlled [*Hawthorne and Rubin*, 2010; *Bartlow et al.*, 2011]. The tremor locations in *Houston et al.* [2011] do provide the required temporal resolution however, to our knowledge, time-dependent changes in slip front advance have not been explored.

[44] A second cause of this apparent correlation could be that the onset of a slow slip front occurs on timescales that are either equivalent to, or greater than tidal timescales. If slip were to nucleate and accelerate to slow slip speeds on timescales much shorter than tidal periods, we would expect to see no tidal dependence of slip nucleation, as LFEs should behave in an aftershock-like manner to the near-instantaneous application of stress. For example, *Shelly and Johnson* [2011] show that LFEs respond to stress transfer from the Parkfield and San Simeon earthquakes with a near-instantaneous increase in event rate. However, if the duration of onset is greater or equal to tidal periods then LFEs may preferentially trigger at times that are tidally favorable. Many slip episodes, like those shown in Figure 2 Family 65, do appear to onset gradually with several hours between the first event within an episode and sustained elevated event rates. This gradual onset of slip events qualitatively supports this hypothesis, as LFE rates during some slip episodes accelerate between the first discernable onset of slip and peak event rate over hourly timescales.

4.3. Tidal Sensitivity and LFE Source Properties

[45] What do the spatial variations in tidal sensitivity reveal about underlying changes in source properties or conditions? Multiple studies have inferred high pore fluid pressures in the tremor source region of subduction zones from high V_p/V_s ratios and the influence of small stress perturbations on tremor rates [*Audet et al.*, 2009; *Shelly et al.*,
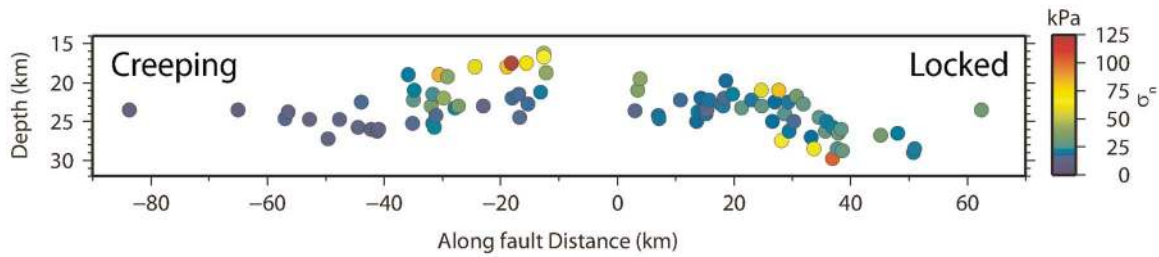
Figure 13. Along fault cross section (identical to Figure 4) with family hypocenters color-coded by effective normal stress derived from equation (1).

2007b]. Laboratory experiments and numerical models of faults with rate and state dependent strength suggest earthquakes have a greater probability of being triggered as the ratio of the oscillatory stress amplitude, τ, to the effective fault-normal stress, σ_n, increases [*Lockner and Beeler*, 1999; *Beeler and Lockner*, 2003]. Since the ratio τ/σ_n for a fixed amplitude perturbation is greater in regions with high pore fluid pressure, low effective stress also provides a potential explanation for the sensitivity of LFEs to extremely small stress changes. We can quantify the effective normal stress required to produce the observed rates of LFE occurrence for each family using the equation

$$R(\tau) = r \exp\left(\frac{\tau}{a\sigma_n}\right) \qquad (1)$$

where $R(\tau)$ is the rate of occurrence of LFEs in response to the tidally induced shear stress τ, r is the average rate of LFE occurrence based on the null hypothesis that LFEs and tides are randomly distributed, a is the rate parameter, and σ_n is the effective normal stress in the LFE source region [*Dieterich*, 2007]. To determine the effective normal stress for each family, we fit equation (1) to the RLSS rate plots discussed in section 3.4 and find the value of $a\sigma_n$ that best describes the data in the least squares sense. We assume a value of 0.02 for a, appropriate for granite at hydrothermal conditions [*Blanpied et al.*, 1995], to produce the effective normal stresses shown in Figure 13. One caveat to this analysis is the constant normal stress assumption. If pore fluid pressures are indeed near lithostatic, fluctuations in tidally induced FNS may be a significant fraction of the effective normal stress in the LFE source region. We discuss the constant normal stress assumption in this calculation in detail in section 4.5, however, considering that most families have significant values of FNS N_{ex}, those correlations are induced by stresses an order of magnitude higher than tidally induced shear stresses suggesting the overall effect of FNS is modest relative to the RLSS.

[46] For the majority of families, our estimates of effective normal stresses are extremely small, averaging around 30 kPa, compared to the ambient lithostatic pressure of 500–700 MPa. The distribution of pore fluid pressure largely reflects that of the RLSS N_{ex} values shown in Figure 4c. Families with the highest RLSS N_{ex} values and lowest effective normal stress estimates cluster to the northwest within the creeping section of the SAF and at greater depths. Values of σ_n gradually increase to near 70 kPa in the shallower families near the Parkfield hypocenter. The average σ_n

value from Figure 13 is five orders of magnitude smaller than values assuming lithostatic overburden and hydrostatic pore fluid pressure. The only parameter in equation (1) capable of varying over multiple orders of magnitude is σ_n, as the tidal stresses and event rates are well constrained and laboratory experiments performed under hydrothermal conditions appropriate for the LFE source region indicate a can vary by at most an order of magnitude between 10^{-2} and 10^{-3} [*Blanpied et al.*, 1995]. This suggests generating LFE rates equivalent to those observed requires near-lithostatic pore fluid pressure to produce effective normal stress values of 10–100 kPa.

[47] Most modeling efforts of transient fault slip focus on SSEs instead of accompanying tremor that represents a small fraction of the total moment released in an episodic tremor and slip event [*Kao et al.*, 2010]. For a synopsis of models explaining slow slip and associated caveats see *Segall et al.* [2010], *Rubin* [2011], and references therein. While the specific model features that give rise to slow slip vary, the common goals of each modeling effort are to (1) nucleate slip without allowing it to accelerate to seismic slip speeds, (2) match, with reasonable variability, the observations associated with SSEs (e.g. slip front propagation speeds, recurrence intervals, size of slipping area, etc.) and (3) not require excessive fine-tuning of initial conditions. High pore fluid pressure is not necessarily required to produce slow slip, however, it is a common feature in models of SSEs as it provides a physical basis for the large dimension of the slipping region and can increase the efficiency of the slip quenching mechanism as in *Segall et al.* [2010]. The relationship between slow-slip and tremor has not been fully explored, and developing quantitative frameworks that explain characteristics of both phenomena are candidate problems for future research efforts [*Beroza and Ide*, 2011].

[48] Conceptual models of slow slip and LFEs generally involve multiple small asperities capable of generating seismic radiation in a region that is otherwise slipping aseismically [e.g., *Ando et al.*, 2010]. Numerical models of slow slip necessitate velocity weakening frictional parameters at large length scales to produce slow slip [*Liu and Rice*, 2005, 2007; *Rubin*, 2008; *Segall et al.*, 2010]. One way to produce aseismic (or not detectably seismic) slip on a velocity weakening fault is through the stiffness. In fault-rock systems the stiffness is a proxy for the size of an asperity. When compared to a reference value, the stiffness determines if an asperity will fail via stick-slip or stable sliding [*Ruina*, 1983; *Rice and Ruina*, 1983]. *Ruina* [1983]

defined the critical stiffness or the boundary between these two end-member behaviors as

$$K_{crit} = \frac{(b-a)\sigma_n}{d_c} \qquad (2)$$

where a and b are the rate and state parameters, σ_n is the effective normal stress, and d_c is a characteristic dimension over which slip evolves. For an asperity with stiffness above this critical value, slip will be stable even with velocity weakening frictional parameters. The actual stiffness of an asperity is

$$K = \frac{CG}{(1-\nu)L} \qquad (3)$$

where G is the shear modulus, ν is the Poisson ratio, L is a characteristic slip dimension, and C is a coefficient close to one assuming a uniform stress drop. Equating the critical stiffness with the stiffness (equations (2) and (3)) gives a formulation for critical slip dimension, above which slip will be unstable. It is worth noting that high pore fluid pressure does not promote slip on small patches, as the minimum slip dimension is inversely proportional to σ_n, so lower effective stress calls for larger slip dimensions. The effective normal stress is, however, the most flexible parameter capable of varying by multiple orders of magnitude.

[49] Unstable slip on small asperities in the presence of substantially elevated pore fluid pressure is still possible, but requires $K_{crit} > K$. While detailed source studies of LFE waveforms have not yet been performed, *Shelly* [2010] estimated between 0.25 and 0.5 mm of slip per episode in one particular family. If we assume average slip of 0.25 mm and a characteristic M_w of 1.6, then for a circular asperity we would expect a typical rupture dimension of ~200 m, corresponding to a stiffness of 180 MPa/m assuming $\nu = 0.25$ and $G = 3 * 10^{10}$ Pa. For the critical stiffness, we fix $b - a$ to be 0.004, take a d_c value of 1 μm from *Marone and Kilgore* [1993], and use an effective normal stress value of 10^5 Pa, we find a critical stiffness value of 400 MPa/m which would allow unstable slip to occur on a typical LFE patch. If instead we use an effective normal stress of 10^4 Pa consistent with average values from Figure 13, then the patch stiffness is greater than the critical stiffness and unstable slip should not occur.

[50] This back-of-the-envelope calculation could be improved in several ways, which may reconcile theory and observation. *Fletcher and McGarr* [2011] estimated moment magnitudes between 1.6 and 1.9 for eleven tremor events. If the larger magnitudes are representative, they would perhaps correspond to a larger slip dimension, reducing the patch stiffness to values below the critical value for our estimated normal stress values in Figure 13. Second, it is possible that LFEs within the same family actually correspond to slip on multiple asperities separated by distances below the spatial resolution of the location procedure. If this were true, the analysis related to Figure 13 may overestimate the pore fluid pressure. However, pore fluid pressure is likely still close to lithostatic as *Thomas et al.* [2009] analyzed a catalog of tremor envelopes made up of many constituent LFEs and still found near-lithostatic pore fluid pressure. Third, while variations in stiffness can be responsible for LFE production, it

is worth noting that other factors can influence the transition between stable and unstable sliding. For example, *Gu et al.* [1984] point out that nominally stable regions can have unstable slip if loading rates are high. Finally, equation (1) was derived using a model that considers the effect of sustained periodic loads on a stuck asperity on a slipping fault [*Dieterich*, 1987; *Beeler and Lockner*, 2003]. We use this relationship because it seems to do well in describing tidal triggering of regular earthquakes [e.g., *Cochran et al.*, 2004] and it provides a means of estimating effective normal stress using seismicity rate variations. However, this model may not be applicable to many LFE families or to LFEs in general because it neglects the important effect of coupling between the tides and surrounding fault creep. If the effect of fault creep were considered, the effective normal stress values presented in Figure 13 could be revised upwards and hence represent a lower bound. While the specific values of effective normal stress are model dependent, high pore fluid pressure is one of the only mechanisms capable of explaining the extreme sensitivity of LFEs to small tidally-induced shear stresses and are likely present on the deep SAF. In sections 4.4 and 4.5, we continue to discuss the application of the model behind equation (1) to LFEs noting both when it succeeds and fails to predict our observations. In ongoing work, we are pursuing more detailed models of the influence of fault creep on LFE nucleation.

[51] To summarize, we find effective normal stresses of ~30 kPa near Parkfield using the response of LFEs to tidal stress perturbations. Elevated pore fluid pressures seem to be an omnipresent characteristic of NVT/LFE source regions, but low effective normal stress does not facilitate unstable slip on small asperities as reduction in effective stress can reduce the critical stiffness for seismic slip to below the asperity stiffness. Low effective stress may promote slow slip, however, which would generally explain why slow slip has been observed without NVT, but NVT has not been observed without slow slip. Parkfield is the notable exception as no surface deformation signal associated with tremor activity has been detected with existing instrumentation. However, *Smith and Gomberg* [2009] found that even M5 events at 15 km depth may not produce a geodetically detectable strain signal at the surface. Additionally, the correlated slip histories of a number of shallow families strongly suggests that slow slip occurs in Parkfield [*Shelly*, 2009].

4.4. Implications for Frequency Dependent Friction of LFE Sources

[52] Why are LFEs so strongly correlated with tidal stresses while earthquakes are not? Theoretical and laboratory studies on tidal modulation of earthquakes were able to explain the weak, oftentimes ambiguous correlation of earthquakes with tides as resulting from the inherent time dependence of earthquake nucleation [*Lockner and Beeler*, 1999; *Beeler and Lockner*, 2003]. *Beeler and Lockner* [2003] found that the amplitude of a given periodic stress, and its period relative to the nucleation timescale, governed by the in situ properties of the earthquake source region, dictate whether the stress perturbation is capable of modulating event occurrence. The duration of nucleation is defined as, $t_n = 2\pi a\sigma_n/\dot{\tau}$, where $\dot{\tau}$ is the stressing rate [*Beeler and Lockner*, 2003]. The nucleation timescale represents the amount of time required for the slip velocity to evolve to

seismic slip speeds and also defines the boundary between two frequency-dependent regimes of how earthquake failure time is influenced by sustained periodic stressing such as due to the solid earth tides. In the low-frequency, long period regime (i.e., oscillatory stress period > t_n), events are effectively characterized by threshold failure because the nucleation timescale is much shorter than the period. Once the stress threshold is breached, earthquakes nucleate and occur immediately (with respect to the period of the loading function) and fault strength is effectively constant throughout the nucleation process. Events preferentially correlate with peak loading rates in this regime, as the greatest probability of being triggered occurs at times when stress is increasing fastest. In the high-frequency regime, nucleation times are long with respect to the period of the load, and the loading function controls the evolution of fault strength. Fault strength depends positively on slip rate, resulting in a higher probability of failure when stressing amplitude is positive. Laboratory experiments exploring the effect of increasing fluid pressure on t_n validate the proportionality between the two [*Bartlow et al.*, 2010].

[53] Our observations of a first-order correlation with stress amplitude (high frequency regime) suggest tidal periods are shorter than the nucleation timescale for LFEs. Additionally, the effective stress calculation (equation (1)) inherently assumes a t_n greater than tidal periods [*Beeler and Lockner*, 2003]. We determine if the observed correlation with amplitude is consistent with the Beeler and Lockner framework by computing the nucleation timescale for LFEs in Parkfield. We again let $a = 0.02$, relevant for hydrothermal conditions in the deep crust [*Blanpied et al.*, 1995], and use an effective normal stress of 10^5 Pa. We calculate a stressing rate by taking the product of the stiffness of a characteristic LFE asperity and the background fault slip rate V_l. Combining the 180 MPa/m stiffness calculated in section 4.3 with the 33 mm/yr average deep slip rate estimate of *Ryder and Bürgmann* [2008], we find a value of $t_n = \sim 18$ hours. Since this timescale is longer than the predominant 12.4 hour tidal period, the *Beeler and Lockner* [2003] model predicts that tidal stressing magnitude should modulate LFE rate consistent with our observations. It is worth noting that this value is much smaller than the nucleation time of >1 year calculated by *Beeler and Lockner* [2003] for shallow earthquakes, which may be important for explaining the observed differences in tidal triggering between earthquakes and LFEs.

[54] While the *Beeler and Lockner* [2003] model is seemingly appropriate, there are a few additional factors that limit its general applicability to LFEs. First, while the above calculation is consistent with effective normal stresses of 10^5 Pa, using the average effective normal stress of 10^4 Pa from Figure 13 yields a t_n of ~ 1.8 hours which would put LFEs into the threshold regime where a correlation with peak stressing rate, not stress amplitude, should be observed. One possible explanation for this contradiction is that effective normal stress estimates in Figure 13 are underestimates, as discussed in section 4.3. Second, many LFEs, in particular those in the highly episodic families, have recurrence intervals less than the calculated nucleation time. This is likely due to the assumption that the stressing rate is constant and proportional to the plate velocity which is almost certainly untrue for the most episodic families as the highly variable inter-episode event rates suggest that the stressing rate is

orders of magnitude higher during episodes than between episodes.

[55] In summary, we find that previously theorized frameworks for earthquake nucleation in response to periodic loads are consistent with our primary findings that LFEs correlate with stress amplitude if the duration of slip nucleation for tremor is slightly larger than the tidal period. However, they may not be capable of explaining all of the observations associated with tidal triggering of LFEs, such as the weaker rate dependences and LFE repeat times that fall well below the calculated nucleation timescale.

4.5. Negative Shear Stress Rate Dependence of Failure Times

[56] There are multiple potential explanations for the approximately half hour phase shift in the distribution of failure times relative to the peak tidal shear stress described in section 3.6. The majority of LFE families exhibit a correlation with negative dRLSS (Figure 4e) that does not appear to be due to correlation with other stress components (Figure 5). One possible source of this time delay is the tendency for LFEs to occur in multievent episodes sometimes involving hundreds of events. Such episodes, if generally initiated at peak shear stress, may cause LFE activity initiated at a tidally optimal time to continue into a time that is less tidally favorable. However, if clustering is responsible for the bulk phase shift we would also expect a correlation between the tendency of an LFE family to cluster and phase shift. We note that the highly episodic, shallow families with relatively low RLSS N_{ex} values generally have insignificant correlation with dRLSS. Qualitatively there does not seem to be any correlation between the existence/magnitude of a phase shift and episodicity so clustering cannot be solely responsible for the observed phasing in all families.

[57] Alternatively, the phase shift in Figure 11 may partially reflect how the background loading rate influences the timing of LFEs in response to the cyclical tidal load. We consider a simple threshold failure model for asperity strength with a stressing function consisting of a superposition of the background plate velocity plus a periodic load

$$\tau(t) = kV_lt + A\sin(2\pi t/t_w) \qquad (4)$$

where τ is the stress, and A is a constant amplitude and t_w the period of the cyclical load. In this failure model, LFEs can only occur when the stressing function exceeds some stress threshold. If the background stressing rate is larger than the maximum tidal stressing rate, the stressing function is monotonically increasing and LFEs can occur during all times of the tidal cycle. If the background loading rate and the peak tidal stressing rate are of comparable magnitude, LFEs can only occur once the stressing function has emerged from the "stress shadow" of the previous cycle during which the net loading rate becomes negative. In this case, for a constant background loading rate, the peak in the stressing function occurs slightly after the peak in the tidal stressing function alone [*Lockner and Beeler*, 1999]. Since we measure LFE rates relative to only the tidal component, and not the overall loading function, it is possible that the slight phase delay is a manifestation of the magnitude of the background loading rate. If we let $A = 100$ Pa, the mean tidal shear stress amplitude, $t_w = 12.4$ hours, stiffness $k = 180$ MPa/m, and assume

that the peak loading amplitude should correspond to peak LFE rate, we find that a loading velocity, V_l, three orders of magnitude smaller than the 33 mm/yr deep slip rate reported by *Ryder and Bürgmann* [2008] is required to match the half hour phase shift. Additionally, for constant V_l and tidal amplitude A, this model predicts that no LFEs should occur while the net loading rate is negative following each cyclical load peak, which directly contradicts our observations. However, tidal amplitudes are not constant and the episodic nature of most LFE families suggests that fault slip rates are highly variable. If these additional complexities were incorporated into equation (4), then the model may be able to reproduce the observed phase delays (Figure 11), while also producing failure times at all phases but predominantly correlated with amplitude.

[58] A third potential cause of the phase shift in Figure 11 could be fluctuations in tidally-induced normal stress. Our findings indicate that LFEs are most sensitive to RLSS however most families have a weaker, yet still significant correlation with FNS. Despite the fact that tides are primarily volumetric stresses and cause normal stress changes nearly an order of magnitude larger than shear stresses, neither of the studies that explore the dependence of earthquake failure times on periodic stress consider variations in normal stress [*Dieterich*, 1987; *Beeler and Lockner*, 2003]. While constant normal stress is likely a reasonable assumption for shallow faults, the environments that are most likely to experience tidal modulation of earthquakes (i.e. where the effective confining stress is low) are also those where the fluctuations in normal stress induced by the tides are likely to have the greatest impact. An exploration of the characteristics of a model like that of *Beeler and Lockner* [2003] incorporating normal-stress fluctuations is beyond the scope of the current study. However, we speculate that normal stress oscillations may play an increasingly important role in the timing of slip in environments with substantially elevated pore fluid pressures.

4.6. Fault Geometry at Depth and Correlation of Tremor With Fault-Normal Compression

[59] While the 88 hypocentral locations are too sparse to map details of fault geometry to depth over the 160 km section of the SAF, the majority of locations seem to lie on one coherent fault strand with very few events deviating substantially from the mapped trace (Figures 1 and 10). The locations of the LFEs between Parkfield and Cholame closely follow a bend in the SAF surface trace suggesting a similar first-order geometry from the surface to near the base of the crust. This observation suggests that while some small amount of the total slip budget may be accommodated off-fault, tremor-producing deformation largely remains localized at depths up to 25 km, and the geometry of closely spaced hypocenters may reflect the geometry of the SAF at depth. If the majority of LFE hypocenters are on the fault, the similar morphology of both the LFE hypocentral locations and the mapped fault trace within the surface fault-bend region (Figure 10) suggests that the bend is preserved at depth.

[60] The SAF fault geometry and localized deformation continue to depths well below the base of the seismogenic zone at temperatures and pressures that suggest that deformation should be by distributed ductile deformation [*Bürgmann and Dresen*, 2008]. If near lithostatic pore fluid pressures are present in the LFE source region, they provide a potential mechanism for sustaining localized slip in the lower crust. Typically, deformation transitions between brittle and ductile at the depth that strength (differential stress) derived from Byerlee's law exceeds the strength from an Arrhenius-type flow law with parameters appropriate for the region of interest. If pore fluid pressure increases dramatically below the brittle-ductile transition, then brittle failure would remain the preferred mode of deformation as increased fluid pressures dramatically reduce the effective friction coefficient, lowering the differential stress required for brittle failure, and increasing the depth of the transition between brittle and fully ductile deformation.

[61] Conventional models of crustal rheology suggest that below the brittle-ductile transition deformation delocalizes from a narrow fault zone to a wider zone of more distributed shear due to the onset of plasticity in the mineral constituents of the host rock [*Bürgmann and Dresen*, 2008]. Exhumed mid-crustal shear zones along the Alpine fault in New Zealand [e.g., *Little et al.*, 2002] and the Liquine-Ofqui fault in Chile [e.g., *Cembrano et al.*, 2002] provide structural evidence of ductile flow between 20–30 km depth under pressure and temperature conditions that are likely similar to those on the deep SAF. These deep shear zones are generally characterized by mylonitic fabrics that are progressively overprinted by more localized regions of ductile shear, and then brittle faulting during exhumation. While exhumed faults do display evidence of ductile flow, one striking observation common to both of the examples is that the zone of distributed shear is relatively narrow: less than 5 km on the Liquine-Ofqui fault and 1–2 km on the Alpine fault and much of the deformation appears highly localized in even narrower ultra-mylonitic shear zones. These observations also suggest that deep, yet localized deformation on continental transforms may be more common than previously thought.

[62] Local fault geometry may also provide a potential explanation for the correlation of a cluster of families with negative FNS (Figure 4b). Figure 14 compares the strike of the SAF to the FNS N_{ex} values for all families. The dramatic change in strike between N43°W and N30°W occurs over a distance of ~10 km on a section of the SAF in the Gold Hill region between Parkfield and Cholame [*Simpson et al.*, 2006; *Bilham and King*, 1989]. The location of this releasing right bend, indicated in red, correlates well with the locations of negative FNS N_{ex} values. Further evidence for the bend at depth can be found in the optimal orientations for tidal correlation shown in Figure 11. If we compare the mean orientations for families with statistically significant negative values of FNS to those of the entire population we find that for both the $\mu = 0.0$ and $\mu = 0.1$ cases, orientations that maximize N_{ex} are rotated clockwise by an average of 4° and 8° respectively.

[63] The presence of the fault bend at depth may also relate to the mechanically implausible correlation with clamping of a number LFE families (Figure 4b, negative FNS families). In conventional frictional failure models, earthquakes should preferentially occur during times of reduced fault-normal stress making this a surprising finding. The hypothesis testing results discussed in section 3.2 indicate that the significant negative FNS values are not an artifact of correlation with another stressing function (see families 41, 44, 45, and
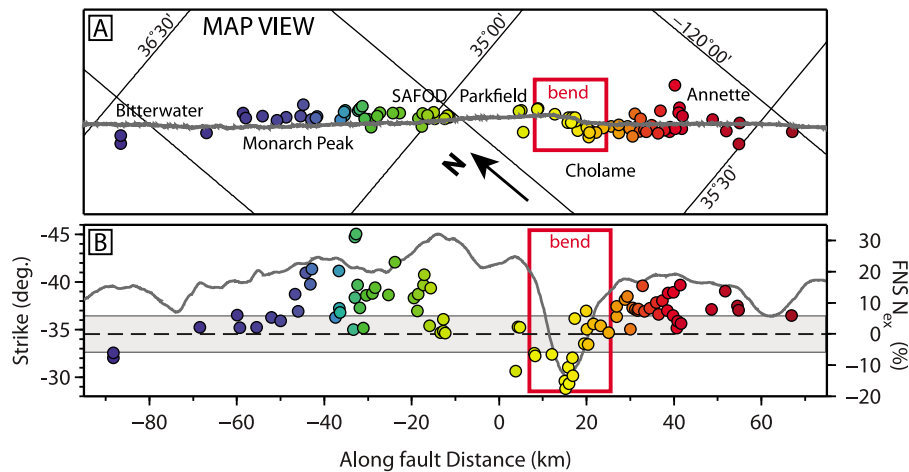
Figure 14. (a) A rotated map view of LFE locations color-coded by family ID number as in Figure 1. The fault bend region is outlined in red to highlight the common morphology of the surface fault strike and the LFE hypocentral locations at depth. (B) The mapped fault strike, dark gray solid line, in degrees west of north (left axis) derived from the strike in panel A as a function of distance along the fault. Colored circles correspond to families in Figure 14a. Their vertical position, measured relative to the right axis, is their FNS N_{ex} value. Dark gray dashed line marks the zero FNS N_{ex} value with 99% confidence intervals indicated in light gray.

49–57 in Figures 5 and S1). As each LFE family is analyzed as an independent data set and all families are compared to the same stressing functions the spatial concentration of the families with negative N_{ex} values also supports the hypothesis testing results.

4.7. Evidence for Evolution of Effective Contact Area

[64] In section 4.3, we appealed to near-lithostatic values of pore fluid pressure to explain the robust sensitivity of LFEs to tidally-induced RLSS and the relatively low to insignificant FNS N_{ex} values. While this framework is consistent with our observations of tidal triggering in most families, it cannot explain the robust correlation of several families with both tensile FNS and RLSS. These families, labeled positive FNS families in Figure 4b, are somewhat paradoxical in that they have RLSS N_{ex} values of ~30% indicative of elevated pore fluid pressures, yet they also have FNS N_{ex} values of ~25%, suggesting that the fault may no longer be desensitized to normal-stress changes. However, if the fault is once again sensitive to normal stress, then how is it possible for it to feel the effect of small RLSS changes in the presence of an overburden pressure of hundreds of megapascal?

[65] One potential mechanism for this may be the evolution of the real area of contact across the fault with depth. *Scholz* [2002] suggested an effective stress law for friction of the form

$$\sigma_n = \sigma - (1 - A_r/A)p \qquad (5)$$

where A_r is the area of contact in the fault zone, A is the total area of the fault, σ is the applied normal stress, and p is the pore fluid pressure. The $\alpha = 1 - A_r/A$ factor measures the sensitivity of effective stress to pore pressure and reflects the influence of fault topography. When two surfaces with roughness are put in contact, they physically touch on contact points known as asperities. At low normal stress such as for

shallow fault zones, the sum of the areas of all these asperities (A_r) is generally only a very small fraction of the total fault area (A), so if $A_r \ll A$, the effective normal stress can be approximated as the normal stress minus the pore fluid pressure. As depth increases, the real area of contact increases, and asperities within the fault zone bear a progressively larger fraction of the load. Thus for shallow faulting α is near one and the effective stress is determined by how effectively changes in pore fluid pressure can buffer changes in applied stress. In a similar model, *Hawthorne and Rubin* [2010] found that for reasonable choices of parameters, the change in pore fluid pressure was greater than 90% the change in applied normal stress. At great depths where rocks begin to deform ductily, α tends toward zero, and effective stress becomes insensitive to the absolute level of pore pressure. Accordingly, if the pore pressure between the base of the seismogenic zone and the Moho is nearly lithostatic, as suggested by the dramatic effect small magnitude shear stresses have on LFE occurrence, families that correlate with FNS at depth would be those in regions where the real area of contact approaches the entire fault area.

[66] Figure 15 is a schematic diagram showing the influence of both near-lithostatic pore fluid pressure and changes in effective contact area on crustal strength. The colors correspond to different layers representing the brittle section of the crust which extends between the surface and 15 km, the transition zone between 15 and 30 km depth, and a nominally ductile region below the Moho at ~30 km depth. We have no direct constraints about the nature or degree of localization of deformation in the upper mantle below Parkfield, but post-seismic deformation studies across the western US suggest that upper mantle deformation is by distributed ductile flow in a hot and hydrated asthenosphere [*Bürgmann and Dresen*, 2008]. In the left panel in Figure 15, we specify a pore fluid pressure profile that transitions from hydrostatic to near-lithostatic at the top of the transition zone, consistent with our inferences in section 4.3. On the basis of laboratory
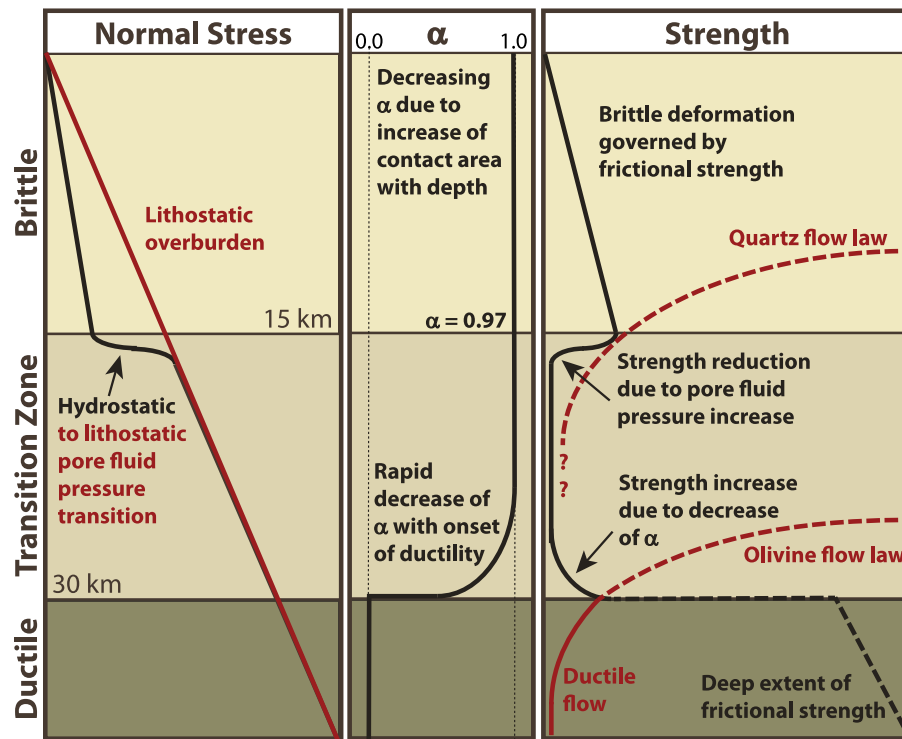
Figure 15. A schematic diagram of normal stress, effective contact area, and strength as a function of depth.

experiments *Dieterich and Kilgore* [1996] argue that A_r/A increases linearly and is approximately equal to the effective normal stress divided by the indentation hardness of the material. If we assume a quartz indentation hardness of 12,000 MPa[*Dieterich and Kilgore*, 1994], α should decrease linearly between one at the surface to around 0.97 at the top of the transition zone as shown in the central panel of Figure 15. The shape of the α curve within the transition zone is largely speculative, as there are few laboratory studies of frictional behavior or effective contact area under pressure and temperature conditions approaching those in the environments that host LFEs. However, we expect that as temperature increases contact area will rapidly increase as thermally activated creep mechanisms increasingly help accommodate rock deformation.

[67] The right panel in Figure 15 shows a hypothetical crustal strength profile incorporating near-lithostatic pore fluid pressures and changes in effective contact area shown in the left and central panels. Frictional strength within the brittle, seismogenic zone increases with pressure and depth in accordance with Byerlee's law. At the top of the transition zone, pore fluid pressures transition between hydro-and lithostatic causing a drastic reduction in strength. While brittle failure is the preferred mode of deformation within the transition zone, as evidenced by the existence of LFEs, the specific deformation mechanism at the top of the transition zone is determined by the depth and degree of pressurization. If the transition between hydro and lithostatic pore pressure takes place above the intersection between the frictional strength envelope and the flow law derived using appropriate parameters (strain rate, material properties, etc.) then frictional failure, rather than flow, is likely the dominant

deformation mechanism between the surface and the deep transition zone. Within the transition zone near-lithostatic pore fluid pressures make frictional failure dominant until changes in α become significant. As α approaches zero, the fault becomes sensitive to progressively larger fractions of the applied normal stress until the frictional failure is no longer preferred as frictional strength exceeds that of an olivine flow law for the upper mantle. Considering the effects of both near-lithostatic pore fluid pressures and increases in contact area with depth can potentially explain both the statistically significant RLSS N_{ex} values in all families and the subset of deep families that robustly correlate with both shear and normal stresses. High pore fluid pressure also provides a mechanism for sustaining localized, rather than distributed, deformation down to 30 km depth consistent with the discussion in section 4.6.

5. Conclusions

[68] The suite of recently identified fault slip behaviors such as episodic slip, slow slip, non-volcanic tremor (NVT), and low frequency earthquakes (LFEs) complicate idealized models of how faults accommodate deformation [*Ide et al.*, 2007; *Peng and Gomberg*, 2010]. We exploit the extreme sensitivity of LFEs to small stress perturbations to elicit information about the in-situ properties of LFE source regions within the brittle-to-ductile transition.

[69] We map the spatially heterogeneous sensitivity of LFEs to tidally induced fault-normal stress, right-lateral shear stress, and their time derivatives along a 160 km span of the SAF near Parkfield, CA extending from 16 to 30 km depth. We find that LFEs are most strongly influenced by RLSS

with a surplus of LFEs occurring when the tides are promoting slip on the fault. Some families also have significant sensitivity to both positive and negative FNS. The families that correlate with extension generally occur deep in the creeping section, and their correlation may be a manifestation of the increase in effective contact area with depth. Families that correlate with fault normal clamping are spatially localized and coincide with a right-stepping fault bend evident in the surface fault trace. If the change in fault geometry is responsible for the anomalous correlations, it would argue that the San Andreas remains localized to depths near the Moho and that large scale (∼10 km) fault morphology present at the surface is also preserved at depth.

[70] The incontrovertible correlation of high pore fluid pressures and slow slip across tectonic environments suggests a causative relationship between the two. Our analysis suggests low effective stress is required to produce the robust response of LFEs to the tides. It is worth noting, however, that high pore fluid pressures do not facilitate LFE production as decreasing effective stress requires increasing source dimensions to host unstable slip, making unstable slip on small asperities more difficult. The recurrence characteristics of LFEs are some of the few observational constraints illuminating the style of deformation in deep fault zones. We also find a first-order correlation between deformation style and tidally induced RLSS, as highly episodic, shallow families generally have smaller RLSS N_{ex} values than the deeper, continuously deforming families.

[71] The duration and style of loading, and the timing of earthquakes relative to the application of a load is of considerable interest to those studying the roles of static and dynamic stresses in earthquake triggering and the mechanical implications of those observations. We find that the timing of LFEs with respect to tidally induced stresses is consistent with some aspects of a previously proposed model of earthquake triggering in response to tidal loading [*Beeler and Lockner*, 2003]. There are, however, some inconsistencies such as recurrence times less than the computed LFE nucleation time, failure times that correlate with stressing rate, and the neglected effect of fault creep that limit general applicability of the *Beeler and Lockner* [2003] model.

[72] A second order dependence on dRLSS is also present in the phases of triggering times relative to the tidal load. A statistically significant number of LFEs trigger preferentially when RLSS magnitude is positive but decreasing. A number of possible causes could potentially explain the phase shift, including clustering, superposition of the background plate rate and the tidal load, or the weak influence of normal stresses that were not considered in previous models. While our data cannot resolve if slip events in Parkfield are triggered by the tides, the population of events that initiate a slip episode on a particular asperity are tidally correlated, suggesting that tidal forces play a role in slip front propagation speeds, and/or the onset of slow slip pulses is comparable to tidal timescales.

References

Agnew, D. C. (1997), NLOADF: A program for computing ocean-tide loading, *J. Geophys. Res.*, *102*(B3), 5109–5110.

Ando, R., R. Nakata, and T. Hori (2010), A slip pulse model with fault heterogeneity for low-frequency earthquakes and tremor along plate interfaces, *Geophys. Res. Lett.*, *37*, L10310, doi:10.1029/2010GL043056.

Audet, P., M. G. Bostock, N. I. Christensen, and S. M. Peacock (2009), Seismic evidence for overpressured subducted oceanic crust and megathrust fault sealing, *Nature*, *457*, 76–78, doi:10.1038/nature07650.

Bartlow, N. M., D. Lockner, and N. M. Beeler (2010), The effect of water on triggering of stick slip by oscillatory loading meeting, paper presented at Southern California Earthquake Center Annual Meeting, Palm Springs, Calif.

Bartlow, N. M., S. Miyazaki, A. M. Bradley, and P. Segall (2011), Space-time correlation of slip and tremor during the 2009 Cascadia slow slip event, *Geophys. Res. Lett.*, *38*, L18309, doi:10.1029/2011GL048714.

Beeler, N. M., and D. A. Lockner (2003), Why earthquakes correlate weakly with the solid Earth tides: Effects of periodic stress on the rate and probability of earthquake occurrence, *J. Geophys. Res.*, *108*(B8), 2391, doi:10.1029/2001JB001518.

Beroza, G. C., and S. Ide (2011), Slow earthquakes and nonvolcanic tremor, *Annu. Rev. Earth Planet. Sci.*, *39*, 271–296, doi:10.1146/annurev-earth-040809-152531.

Bilham, R., and G. King (1989), The morphology of strike-slip faults: Examples from the San Andreas Fault, California, *J. Geophys. Res.*, *941*, 10,204–10,216, doi:10.1029/JB094iB08p10204.

Blanpied, M. L., D. A. Lockner, and J. D. Byerlee (1995), Frictional slip of granite at hydrothermal conditions, *J. Geophys. Res.*, *100*, 13,045–13,064, doi:10.1029/95JB00862.

Boyarko, D. C., and M. R. Brudzinski (2010), Spatial and temporal patterns of nonvolcanic tremor along the southern Cascadia subduction zone, *J. Geophys. Res.*, *115*, B00A22, doi:10.1029/2008JB006064.

Brown, J. R., G. C. Beroza, S. Ide, K. Ohta, D. R. Shelly, S. Y. Schwartz, W. Rabbel, M. Thorwart, and H. Kao (2009), Deep low-frequency earthquakes in tremor localize to the plate interface in multiple subduction zones, *Geophys. Res. Lett.*, *36*, L19306, doi:10.1029/2009GL040027.

Brudzinski, M. R., H. R. Hinojosa-Prieto, K. M. Schlanser, E. Cabral-Cano, A. Arciniega-Ceballos, O. Diaz-Molina, and C. DeMets (2010), Nonvolcanic tremor along the Oaxaca segment of the Middle America subduction zone, *J. Geophys. Res.*, *115*, B00A23, doi:10.1029/2008JB006061.

Bürgmann, R., and G. Dresen (2008), Rheology of the lower crust and upper mantle: Evidence from rock mechanics, geodesy, and field observations, *Annu. Rev. Earth Planet. Sci.*, *36*, 531–567, doi:10.1146/annurev.earth.36.031207.124326.

Cembrano, J., A. Lavenu, P. Reynolds, G. Arancibia, G. Lopez, and A. Sanhueza (2002), Late Cenozoic transpressional ductile deformation north of the Nazca-South America-Antarctica triple junction, *Tectonophysics*, *354*, 289–314, doi:10.1016/S0040-1951(02)00388-8.

Cochran, E. S., J. E. Vidale, and S. Tanaka (2004), Earth tides can trigger shallow thrust fault earthquakes, *Science*, *306*, 1164–1166, doi:10.1126/science.1103961.

de Juan, J., et al. (2010), Sudden increase in tidal response linked to calving and acceleration at a large Greenland outlet glacier, *Geophys. Res. Lett.*, *371*, L12501, doi:10.1029/2010GL043289.

Dieterich, J. H. (1987), Nucleation and triggering of earthquake slip: Effect of periodic stresses, *Tectonophysics*, *144*, 127–139, doi:10.1016/0040-1951(87)90012-6.

Dieterich, J. H. (2007), Applications of rate- and state-dependent friction to models of fault slip and earthquake occurrence, in *Treatise on Geophysics*, vol. 4, *Earthquake Seismology*, pp. 107–129, Elsevier, New York, doi:doi:10.1016/B978-044452748-6.00065-1.

Dieterich, J. H., and B. D. Kilgore (1994), Direct observation of frictional contacts: New insights for state-dependent properties, *Pure Appl. Geophys.*, *143*, 283–302, doi:10.1007/BF00874332.

Dieterich, J. H., and B. Kilgore (1996), Implications of fault constitutive properties for earthquake prediction, *Proc. Natl. Acad. Sci. U. S. A.*, *93*, 3787–3794, doi:10.1073/pnas.93.9.3787.

Dragert, H., K. Wang, and T. S. James (2001), A silent slip event on the deeper Cascadia subduction interface, *Science*, *292*, 1525–1528, doi:10.1126/science.1060152.

Dragert, H., K. Wang, and G. Rogers (2004), Geodetic and seismic signatures of episodic tremor and slip in the northern Cascadia subduction zone, *Earth Planets Space*, *56*, 1143–1150.

Fletcher, J. B., and A. McGarr (2011), Moments, magnitudes, and radiated energies of non-volcanic tremor near Cholame, CA, from ground motion spectra at UPSAR, *Geophys. Res. Lett.*, *381*, L16314, doi:10.1029/2011GL048636.

Ghosh, A., J. E. Vidale, Z. Peng, K. C. Creager, and H. Houston (2009), Complex nonvolcanic tremor near Parkfield, California, triggered by the great 2004 Sumatra earthquake, *J. Geophys. Res.*, *114*, B00A15, doi:10.1029/2008JB006062.

Gomberg, J., J. L. Rubinstein, Z. Peng, K. C. Creager, J. E. Vidale, and P. Bodin (2008), Widespread triggering of nonvolcanic tremor in California, *Science*, *319*, 173, doi:10.1126/science.1149164.

Gu, J., J. R. Rice, A. L. Ruina, and S. T. Tse (1984), Slip motion and stability of a single degree of freedom elastic system with rate and state dependent friction, *J. Mech. Phys. Solids*, *32*, 167–196, doi:10.1016/0022-5096(84)90007-3.

Harkrider, D. G. (1970), Surface waves in multilayered elastic media. Part II. Higher mode spectra and spectral ratios from point sources in plane layered Earth models, *Bull. Seismol. Soc. Am.*, *60*(6), 1937–1987.

Hawthorne, J. C., and A. M. Rubin (2010), Tidal modulation of slow slip in Cascadia, *J. Geophys. Res.*, *115*, B09406, doi:10.1029/2010JB007502.

Heaton, T. H. (1982), Tidal triggering of earthquakes, *Bull. Seismol. Soc. Am.*, *72*(6), 2181–2200.

Hill, D. P. (2010), Surface-wave potential for triggering tectonic (nonvolcanic) tremor, *Bull. Seismol. Soc. Am.*, *100*, 1859–1878, doi:10.1785/0120090362.

Hirose, H., K. Hirahara, F. Kimata, N. Fujii, and S. Miyazaki (1999), A slow thrust slip event following the two 1996 Hyuganada earthquakes beneath the Bungo Channel, southwest Japan, *Geophys. Res. Lett.*, *26*, 3237–3240, doi:10.1029/1999GL010999.

Houston, H., B. G. Delbridge, A. G. Wech, and K. C. Creager (2011), Rapid tremor reversals in Cascadia generated by a weakened plate interface, *Nat. Geosci.*, *4*, 404–409, doi:10.1038/ngeo1157.

Ide, S. (2010), Striations, duration, migration and tidal response in deep tremor, *Nature*, *466*, 356–359, doi:10.1038/nature09251.

Ide, S., G. C. Beroza, D. R. Shelly, and T. Uchide (2007), A scaling law for slow earthquakes, *Nature*, *447*, 76–79, doi:10.1038/nature05780.

Kao, H., S.-J. Shan, H. Dragert, G. Rogers, J. F. Cassidy, and K. Ramachandran (2005), A wide depth distribution of seismic tremors along the northern Cascadia margin, *Nature*, *436*, 841–844, doi:10.1038/nature03903.

Kao, H., K. Wang, H. Dragert, J. Y. Kao, and G. Rogers (2010), Estimating seismic moment magnitude (M_w) of tremor bursts in northern Cascadia: Implications for the "seismic efficiency" of episodic tremor and slip, *Geophys. Res. Lett.*, *371*, L19306, doi:10.1029/2010GL044927.

Lambert, A., H. Kao, G. Rogers, and N. Courtier (2009), Correlation of tremor activity with tidal stress in the northern Cascadia subduction zone, *J. Geophys. Res.*, *114*, B00A08, doi:10.1029/2008JB006038.

Little, T. A., R. J. Holcombe, and B. R. Ilg (2002), Kinematics of oblique collision and ramping inferred from microstructures and strain in middle crustal rocks, central Southern Alps, New Zealand, *J. Struct. Geol.*, *24*, 219–239, doi:10.1016/S0191-8141(01)00060-8.

Liu, Y., and J. R. Rice (2005), Aseismic slip transients emerge spontaneously in three-dimensional rate and state modeling of subduction earthquake sequences, *J. Geophys. Res.*, *110*, B08307, doi:10.1029/2004JB003424.

Liu, Y., and J. R. Rice (2007), Spontaneous and triggered aseismic deformation transients in a subduction fault model, *J. Geophys. Res.*, *112*, B09404, doi:10.1029/2007JB004930.

Lockner, D. A., and N. M. Beeler (1999), Premonitory slip and tidal triggering of earthquakes, *J. Geophys. Res.*, *104*, 20,133–20,152, doi:10.1029/1999JB900205.

Marone, C. (1998), Laboratory-derived friction laws and their application to seismic faulting, *Annu. Rev. Earth Planet. Sci.*, *26*, 643–696.

Marone, C., and B. Kilgore (1993), Scaling of the critical slip distance for seismic faulting with shear strain in fault zones, *Nature*, *362*, 618–621, doi:10.1038/362618a0.

McNutt, S. R., and R. J. Beavan (1984), Patterns of earthquakes and the effect of solid earth and ocean load tides at Mount St. Helens prior to the May 18, 1980, eruption, *J. Geophys. Res.*, *89*, 3075–3086, doi:10.1029/JB089iB05p03075.

Miller, M. M., T. Melbourne, D. J. Johnson, and W. Q. Sumner (2002), Periodic slow earthquakes from the Cascadia subduction zone, *Science*, *295*, 2423, doi:10.1126/science.1071193.

Miyazawa, M., and E. E. Brodsky (2008), Deep low-frequency tremor that correlates with passing surface waves, *J. Geophys. Res.*, *113*, B01307, doi:10.1029/2006JB004890.

Murray, J., and J. Langbein (2006), Slip on the San Andreas Fault at Parkfield, California, over two earthquake cycles, and the implications

for seismic hazard, *Bull. Seismol. Soc. Am.*, *96*, S283–S303, doi:10.1785/0120050820.

Nadeau, R. M., and A. Guilhem (2009), Nonvolcanic tremor evolution and the San Simeon and Parkfield, *Science*, *325*, 191–194, doi:10.1126/science.1174155.

Nakata, R., N. Suda, and H. Tsuruoka (2008), Non-volcanic tremor resulting from the combined effect of Earth tides and slow slip events, *Nat. Geosci.*, *1*, 676–678, doi:10.1038/ngeo288.

Obara, K. (2002), Nonvolcanic deep tremor associated with subduction in southwest Japan, *Science*, *296*, 1679–1681, doi:10.1126/science.1070378.

Obara, K. (2010), Phenomenology of deep slow earthquake family in southwest Japan: Spatiotemporal characteristics and segmentation, *J. Geophys. Res.*, *115*, B00A25, doi:10.1029/2008JB006048.

Obara, K., H. Hirose, F. Yamamizu, and K. Kasahara (2004), Episodic slow slip events accompanied by non-volcanic tremors in southwest Japan subduction zone, *Geophys. Res. Lett.*, *312*, L23602, doi:10.1029/2004GL020848.

Peng, Z., and J. Gomberg (2010), An integrated perspective of the continuum between earthquakes and slow-slip phenomena, *Nat. Geosci.*, *3*, 599–607, doi:10.1038/ngeo940.

Peng, Z., J. E. Vidale, A. G. Wech, R. M. Nadeau, and K. C. Creager (2009), Remote triggering of tremor along the San Andreas Fault in central California, *J. Geophys. Res.*, *114*, B00A06, doi:10.1029/2008JB006049.

Rice, J. R., and A. L. Ruina (1983), Stability of steady frictional slipping, *J. Appl. Mech.*, *50*, 343, doi:10.1115/1.3167042.

Rubin, A. M. (2008), Episodic slow slip events and rate-and-state friction, *J. Geophys. Res.*, *113*, B11414, doi:10.1029/2008JB005642.

Rubin, A. M. (2011), Designer friction laws for bimodal slow slip propagation speeds, *Geochem. Geophys. Geosyst.*, *12*, Q04007, doi:10.1029/2010GC003386.

Rubinstein, J. L., M. La Rocca, J. E. Vidale, K. C. Creager, and A. G. Wech (2008), Tidal modulation of nonvolcanic tremor, *Science*, *319*, 186–189, doi:10.1126/science.1150558.

Ruina, A. (1983), Slip instability and state variable friction laws, *J. Geophys. Res.*, *881*, 10,359–10,370, doi:10.1029/JB088iB12p10359.

Ryder, I., and R. Bürgmann (2008), Spatial variations in slip deficit on the central San Andreas Fault from InSAR, *Geophys. J. Int.*, *175*, 837–852, doi:10.1111/j.1365-246X.2008.03938.x.

Schmidt, D. A., and H. Gao (2010), Source parameters and time-dependent slip distributions of slow slip events on the Cascadia subduction zone from 1998 to 2008, *J. Geophys. Res.*, *115*, B00A18, doi:10.1029/2008JB006045.

Scholz, C. H. (2002), *The Mechanics of Earthquakes and Faulting*, Cambridge Univ. Press, Cambridge, U. K.

Schulz, W. H., J. W. Kean, and G. Wang (2009), Landslide movement in southwest Colorado triggered by atmospheric tides, *Nat. Geosci.*, *2*, 863–866, doi:10.1038/ngeo659.

Segall, P., A. M. Rubin, A. M. Bradley, and J. R. Rice (2010), Dilatant strengthening as a mechanism for slow slip events, *J. Geophys. Res.*, *115*, B12305, doi:10.1029/2010JB007449.

Shelly, D. R. (2009), Possible deep fault slip preceding the 2004 Parkfield earthquake, inferred from detailed observations of tectonic tremor, *Geophys. Res. Lett.*, *36*, L17318, doi:10.1029/2009GL039589.

Shelly, D. R. (2010), Periodic, chaotic, and doubled earthquake recurrence intervals on the deep San Andreas Fault, *Science*, *328*, 1385–1388, doi:10.1126/science.1189741.

Shelly, D. R., and J. L. Hardebeck (2010), Precise tremor source locations and amplitude variations along the lower-crustal central San Andreas Fault, *Geophys. Res. Lett.*, *37*, L14301, doi:10.1029/2010GL043672.

Shelly, D. R., and K. M. Johnson (2011), Tremor reveals stress shadowing, deep postseismic creep, and depth-dependent slip recurrence on the lower-crustal San Andreas fault near Parkfield, *Geophys. Res. Lett.*, *381*, L13312, doi:10.1029/2011GL047863.

Shelly, D. R., G. C. Beroza, S. Ide, and S. Nakamula (2006), Low-frequency earthquakes in Shikoku, Japan, and their relationship to episodic tremor and slip, *Nature*, *442*, 188–191, doi:10.1038/nature04931.

Shelly, D. R., G. C. Beroza, and S. Ide (2007a), Non-volcanic tremor and low-frequency earthquake swarms, *Nature*, *446*, 305–307, doi:10.1038/nature05666.

Shelly, D. R., G. C. Beroza, and S. Ide (2007b), Complex evolution of transient slip derived from precise tremor locations in western Shikoku, Japan, *Geochem. Geophys. Geosyst.*, *81*, Q10014, doi:10.1029/2007GC001640.

Shelly, D. R., W. L. Ellsworth, T. Ryberg, C. Haberland, G. S. Fuis, J. Murphy, R. M. Nadeau, and R. Bürgmann (2009), Precise location of San Andreas Fault tremors near Cholame, California using seismometer clusters: Slip on the deep extension of the fault?, *Geophys. Res. Lett.*, *36*, L01303, doi:10.1029/2008GL036367.

Shelly, D. R., Z. Peng, D. P. Hill, and C. Aiken (2011), Triggered creep as a possible mechanism for delayed dynamic triggering of tremor and earthquakes, *Nat. Geosci.*, *4*, 384–388, doi:10.1038/ngeo1141.

Simpson, R. W., M. Barall, J. Langbein, J. R. Murray, and M. J. Rymer (2006), San Andreas Fault geometry in the Parkfield, California, region, *Bull. Seismol. Soc. Am.*, *96*, 28–37, doi:10.1785/0120050824.

Smith, E. F., and J. Gomberg (2009), A search in strainmeter data for slow slip associated with triggered and ambient tremor near Parkfield, California, *J. Geophys. Res.*, *114*, B00A14, doi:10.1029/2008JB006040.

Thomas, A. M., R. M. Nadeau, and R. Bürgmann (2009), Tremor-tide correlations and near-lithostatic pore pressure on the deep San Andreas fault, *Nature*, *462*, 1048–1051, doi:10.1038/nature08654.

Thurber, C., H. Zhang, F. Waldhauser, A. Michael, J. Hardebeck, and D. Eberhart-Phillips (2006), Three-dimensional compressional wave-speed model, earthquake relocations (1966–2005), and focal mechanisms

for the Parkfield, California, region, *Bull. Seismol. Soc. Am.*, *96*, 38–49, doi:10.1785/0120050825.

Vidale, J. E., D. C. Agnew, M. J. S. Johnston, and D. H. Oppenheimer (1998), Absence of earthquake correlation with Earth tides: An indication of high preseismic fault stress rate, *J. Geophys. Res.*, *103*, 24,567–24,572, doi:10.1029/98JB00594.

Waldhauser, F., and D. P. Schaff (2008), Large-scale relocation of two decades of northern California seismicity using cross-correlation and double-difference methods, *J. Geophys. Res.*, *113*, B08311, doi:10.1029/2007JB005479.

Wech, A. G., and K. C. Creager (2011), A continuum of stress, strength and slip in the Cascadia subduction zone, *Nat. Geosci.*, *4*, 624–628, doi:10.1038/ngeo1215.

Wech, A. G., K. C. Creager, and T. I. Melbourne (2009), Seismic and geodetic constraints on Cascadia slow slip, *J. Geophys. Res.*, *114*, B10316, doi:10.1029/2008JB006090.